Material configurations, failure analysis and testing of composite tubes subjected to external pressure in oil well environment

Anders Gundersen

THE NORWEGIAN UNIVERSITY
OF SCIENCE AND TECHNOLOGY
DEPARTMENT OF ENGINEERING DESIGN
AND MATERIALS

MASTER THESIS SPRING 2013
FOR
STUD.TECHN. ANDERS GUNDERSEN

MATERIAL CONFIGURATIONS, FAILURE ANALYSIS AND TESTING OF COMPOSITE TUBES SUBJECTED TO EXTERNAL PRESSURE IN OIL WELL ENVIROMENT

Materialkonfigurasjon, sviktanalyse og testing av komposittrør utsatt for ytre trykk i oljebrønnmiljø

Tubes and rods for well intervention are conventionally deployed into the well by an injector device on the top side. The pushing force must exceed the accumulated friction, pressure, gravitation and drag force from the well fluid. The friction force that is primarily governed by the buoyant weight is identified as the most critical parameter for extended reach in a horizontal well.

A hollowed composite rod may have several advantages, the most important being low submerged weight that reduces the normal contact force in deviated well sections, and thereby reduces the accumulated friction force.

This study shall primarily focus on the behavior of relevant fiber composite tubes subjected to external pressure employing both numerical and experimental methods. The work shall include topics as

- Requirements and scope where principal loads, physical and geometrical constraints, materials, and material configuration are defined
- Evaluation of concepts with primary focus on material efficiency and reliability. Issues such as manufacturing, spooling, operation and maintenance should be briefly addressed
- Simulations and experimental work focusing tubes with simple principal material configuration subjected to external pressure. This task should focus the understanding of fundamental properties, structural failure modes, material failure modes and the application of advanced failure theory such as Puck's failure criteria.
- Optionally, the work may include design of advanced experiments such as combined loading and custom measuring techniques
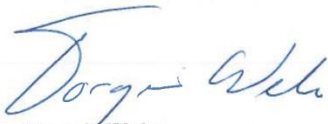
- Based on the results from the principal configurations and absolute requirements, an optimized structure shall be developed.

The thesis should include the signed problem text, and be written as a research report with summary both in English and Norwegian, conclusion, literature references, table of contents, etc. During preparation of the text, the candidate should make efforts to create a well arranged and well written report. To ease the evaluation of the thesis, it is important to cross-reference text, tables and figures. For evaluation of the work a thorough discussion of results is appreciated.

Three weeks after start of the thesis work, an A3 sheet illustrating the work is to be handed in. A template for this presentation is available on the IPM's web site under the menu "Masteroppgave" (http://www.ntnu.no/ipm/masteroppgave). This sheet should be updated one week before the Master's thesis is submitted.

The thesis shall be submitted electronically via DAIM, NTNU's system for Digital Archiving and Submission of Master's thesis.

The contact person is
Nils Petter Vedvik, IPM

Torgeir Welo
Head of Division

Nils Petter Vedvik
Professor/Supervisor

Preface

In this master thesis (TMM 4901) a study about the material behavior of composite tubes subjected to external pressure is conducted. The report is written at the department of product design and materials at the 10th semester. The report is written as a follow-up from the specialization project *Composite rod for well intervention* and is partly written in collaboration with Bernt Christian Braaen. That specialization project was written in the 9th semester, and is the foundation for this work.

All experimental work is done together with Bernt; hence these parts are almost identical in our theses. Parts of the text material and some experimental results in this thesis are taken from the project written fall 2012.

Acknowledgements

First of all, I would like to thank my family for all their support throughout my years as a student. Knowing that there always is someone there for me for guidance and advice has given me an indescribable comfort and confidence through the years.

I would also thank Bernt Christian Braaen for the good collaboration during the years at the university, and especially these past two semesters.

The staff at the department of product design and materials deserves also my gratitude for their guidance and availability.

Of course I would also like to thank my supervisor, Associate Professor Nils Petter Vedvik, for all the help and guidance I needed throughout the semester in order for me to complete this project.

Stud.techn. Anders Gundersen, Trondheim, June 2013

Abstract

Carbon fiber reinforced polymers is an advanced material with unique material properties that is being used more and more in the subsea and petroleum industry. Well intervention is one of many well suited applications for hollow carbon fiber reinforced tubes. Due to the material's properties, the composite material is well suited for many applications when dealing with conditions similar to the environment inside an oil well. It has a much higher stiffness to weight ratio than most materials, great thermal resistance and it is less subjected to fatigue. The material is non-corroding and may be designed for chemical resistance which is a huge benefit in the harsh conditions found for example subsea or in a well. The dominating load in an oil well environment is the extreme pressure. Carbon fiber reinforced polymers is a very strong material, and by customizing its laminate layup, its full strength can be utilized for any loadcase it may be subjected to.

The main focus of this task was to study the behavior of relevant thick-walled fiber composite tubes subjected to external pressure employing both numerical and experimental methods. Three principal composite layups were analyzed, both numerically and experimentally by high pressure testing and axial compression tests. Test samples were produced and evaluated for these tasks, and compared with results from representative finite element models.

Test samples with [±80°], [±45°] and [±80°,±9°] layups were analyzed. The experimental work for the [±80°] samples was done in a previous work, and only the results were presented in this thesis. The samples for the high pressure testing were 150mm long, and the outer and inner diameters were 15mm and 12mm, respectively. The same diameters were used for the axial compression samples, but the length was reduced to 20mm. The dimensions were determined by conventional design criteria for well intervention. The samples were produced by using the filament winding machine at NTNU, and an epoxy bath was used for impregnation.

Puck's failure criterion was implemented in the numerical calculations for material failure prediction. An eigenvalue buckling analysis procedure was conducted for buckling failure prediction. All samples for both test methods failed very close to the predicted failure loads with relatively low percentage difference. The differences were found to be between -11.1% and 12.7%, and a discussion was conducted on possible sources of deviation.

Due to the low deviation between predicted and factual failure loads, it could be concluded that the assumed strength and elasticity parameters of the material was reasonable and that the experimental testing procedures was well fitted for the study of the behavior of composites subjected to compression.

Based on these results, a discussion of an optimized structure was conducted. The geometry analyzed in this thesis had much higher buoyancy than desired for the application. It could thus be concluded that the material has a great potential for the use in oil-well environment.

Sammendrag

Karbonfiber kompositter er avanserte materialer med unike egenskaper som blir brukt mer og mer for applikasjoner i subsea- og petroleumsindustrien. Brønnintervensjon er en av mange bruksområder som passer bra for karbonfiber rør. På grunn av materialets egenskaper og styrke, er materialet godt egnet til applikasjoner der forholdene ligner miljøet inni en oljebrønn. Det har mye høyere stivhet til vekt ratio enn de fleste materialer, har superb termisk motstand og blir ikke påvirket av signing. Materialet korroderer ikke og er veldig kjemisk motstandsdyktig. Dette er egenskaper som har store fordeler under tøffe forhold, som for eksempel på dypt vann eller i en brønn. Den dominerende lasten i oljebrønnmiljø er det ekstreme trykket. Karbonfiber kompositter er veldig sterke materialer, og ved å tilpasse laminatets layup, materialets fulle styrke kan utnyttes til å passe enhver lastkombinasjon.

Hovedfokuset i denne oppgaven var å studere oppførselen til relevante tykk-veggede fiber kompositt rør utsatt for ytre trykk ved å bruke både numeriske og eksperimentelle metoder. Tre prinsipielle kompositt layuper ble analysert, både numerisk og eksperimentelt ved høytrykk testing og aksielle kompresjonstester. Prøvestykker ble produsert og vurdert for disse oppgavene, og representative finite element modeller ble digitalt modellert og kalkulert for sammenligning.

Prøvestykker med [±80°], [±45°] and [±80°,±9°] layups ble analysert. Det eksperimentelle arbeidet for [±80°] prøvene ble gjort i tidligere studie, så kun resultatene av disse ble presentert i denne oppgaven. Prøvene for høytrykkstestingen var 150mm lange, og de ytre og indre diameterne var henholdsvis 15mm og 12mm. De samme diameterne ble brukt for aksial kompresjonstestingen, men lengdene var her redusert til 20mm. Dimensjonene ble bestemt av konvensjonelle design kriterier for brønnintervensjon. Prøvene ble produsert med viklemaskinen på NTNU og et epoxy bad ble brukt for impregnering.

Pucks feilkriterie ble implementert i de numeriske beregningene for å predikere materialsvikt. Beregninger for predikert knekklast ble gjort ved å finne eigenverdiene til rørene. Alle prøver for begge testmetodene sviktet svært nær de predikerte sviktlastene med relativ lav prosentvis forskjell. Forskjellene ble funnet til å ligge mellom -11.1% og 12.7% og det ble gjort en diskusjon på eventuelle feilkilder.

Grunnet de lave forskjellene mellom predikterte og eksperimentelle sviktlaster, kunne det konkluderes at materialets forventede styrke og stivhets parametere var stemte, og at de eksperimentelle testprosedyrene var godt egnet til å studere oppførselen til kompositter utsatt for kompresjon.

Basert på disse resultatene ble en optimalisert struktur diskutert. Geometrien som ble analysert i denne oppgaven hadde mye større oppdrift enn det som er ønsket for bruksmåten. Det kunne dermed bli konkludert at materialet har et stort potensiale for bruk i oljebrønnmiljø.

Table of Contents

List of figures

List of Tables

1 Introduction

1.1 General introduction

Oil and gas will be the number one most important source of energy in the world for years to come. According to the International Energy Agency, the world produced approximately 4100 million tons of crude oil and 3388 billion cubic meters of natural gas in 2011. For the oil production, only a fraction of the existing oil in the fields is producible. This fraction, the recovery factor, defines the size of the reserve, thus the amount of oil that can be brought to the surface. The estimated worldwide recovery factor was on average 35% in 2008, and a one percentage point increase would add 6% to the proven oil reserves in the world (80 billion barrels) [1].

New technologies are needed to increase the recovery factor of existing and future oil reserves. Production optimization and recovery increase is only possible with improved reservoir knowledge. This knowledge can be obtained by well intervention, which provides important information about the performance, environment, state and geometry of the well.

One big limitation for well intervention is the reach. Directional and horizontal drilling creates wells that may be thousands of meters long. This is done to increase the length of the payzone, improve productivity, reach targets that cannot be reached by vertical drilling and to reduce surface footprint. This means that by developing new technologies for well intervention equipment, there is also an ecological compensation to further exploitation of existing and future fields.

Well intervention is a term used about all work being done in an oil or gas well. When it comes to measuring the temperature and the flow profile of the well, different methods are developed; a solid carbon fiber reinforced polymer (CFRP) rod, wireline and coil tubing.

The CFRP rod has several advantages over its competitors, but the performance can be further improved for use in the horizontal sections of the well. As a solid CFRP rod, the submerged weight causes the rod to hit the bottom of the casing, generating friction which prevents the desired reach. By making the rod hollow, the submerged weight will reduce significantly and the rod will stay buoyant in the casing, hence extending the reach.

1.2 CFRP in oil well environment

Well intervention is one of many well suited applications for hollow CFRP tubes. Due to the material's properties, CFRP is well suited for many applications when dealing with conditions similar to the environment inside an oil well. It has a much higher stiffness to weight ratio than most materials, great thermal resistance and it is less subjected to fatigue. The material is non-corroding and may be designed for chemical resistance which is a huge benefit in the harsh conditions found for example subsea or in a well. The dominating load in an oil well environment is the extreme pressure. CFRP has high strength, and by customizing its laminate layup, its full strength can be utilized for any loadcase it may be subjected to.

The industrial need for better defined and more specialized properties for materials with extreme pressure capacities has increased the past few decades. The interest of utilizing fiber reinforced composites properties in the maritime and petroleum industry started in the early 1990's. With the expansion of this industry, a need for studies of the material's capacity and behavior when subjected to such extreme pressures is more and more relevant.

When analyzing and predicting the failure of thick-walled composite tubes subjected only to external pressure it is important to determine at which critical pressure an ideal tube will fail. Experimental tests will result in another failure pressure. This failure pressure is governed by several factors on both material level and structural level. The material contains a multiplicity of characteristics influencing the failure mechanism. While the stiffness and strength properties of the material directly affect the stress state and the failure mode, it is also important to quantify the effect of shape imperfections and examine the tube for microscopic errors. These errors may have great impact on the failure pressure and an investigation provides important information on the quality of the material due to the production method.

At the structural level, the tube is subjected to a complex three dimensional stress state. This fact is of great importance when dealing with anisotropic materials. An appropriate phenomenological failure criterion is thus needed for a detailed analysis when predicting material failure.

During the background research for this thesis it was found that very little work has been carried out on the subject on using failure criteria when predicting failure of composite materials in a pure compressive state. It was found that most work on failure prediction of composite tubes was carried out on thin-walled cylinders, such as the work of H. Rasheed and O. Yousif (2001) [2] and the work of S. Gohari, A. Golshan, M. Mostakhdemin, F. Mozafari, and A. Momenzadeh (2012) [3]. It is known that the most critical failure mechanism for this problem is buckling/collapse. This is especially the fact when dealing with thin-walled tubes due to less structural stability and the vulnerability of shape imperfections. It was also not easy to find relevant studies where advanced failure criteria were applied.

This study primarily focused on the study of principal structural and material mechanisms of thick-walled CFRP tubes subjected to uniform external pressure. Well intervention was used as the application of example. An approach for predicting structural failure was developed by using both numerical and experimental methods. This included an investigation of tube geometry, material properties, composite layups, failure mechanisms and microscopic material errors due to fabrication. With this approach, an evaluation of an optimized structure for the given loadcase was conducted.

The CFRP tubes were analyzed by investigating relevant test samples with different composite layups. Experimental samples were produced, tested, analyzed and compared with ideal numerical models to document material efficiency and reliability.

2 Problem description and failure theory

A numerically calculated ideal critical failure pressure, P_{cr}, was to be found for two sets of samples. These sets of samples were also produced and experimentally tested with two different test methods; high pressure testing and axial compression testing. The results of these tests, the failure pressures P_f, were than compared and evaluated.

The test sample configuration and layup details are shown in Figure 2-1. The inside diameter D_i was 12 mm, and the outside diameter D_o was 15mm. This gave a cylinder thickness t of 1.5mm. The lengths of the high pressure testing samples, L, were 150mm, and 20mm for the axial compression test samples. Three different composite layups were analyzed, which consisted of orthotropic CFRP layers of equal thickness. The stacking sequences were $[\pm80°]_n$, $[\pm45°]_n$ and $[\pm80°_{n/2}/\pm9°_{n/2}]$ where n is an unknown integer, dependent on the production method. For the high pressure tests, the external pressure P_e was applied both in the negative radial direction of the samples, and on the negative axial direction. The axial compression test samples were subjected only to P_e in the axial direction. Atmospheric pressure was obtained on the inside of the samples. Testing was conducted at room temperature (=20°C).
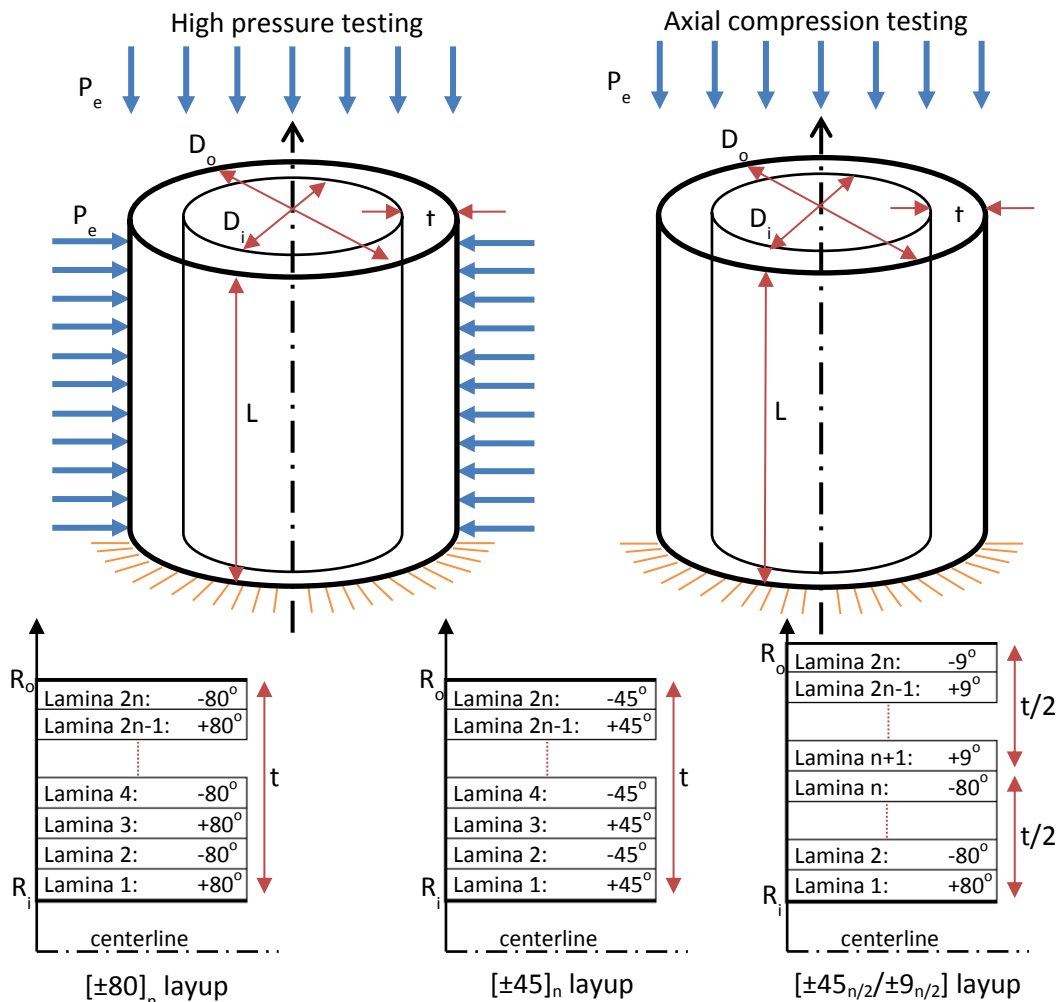
Figure 2-1: test sample configuration and layup details

The dimensions, loads and composite layup configurations were chosen based on the following discussions.

2.1 Design criteria

The test samples were designed by conventional criteria for well intervention. At the same time the samples had to be designed with regard to the production method of the samples and equipment used during the experimental testing.

2.1.1 Geometric constraints

Existing operational injection tools used on topside are designed to operate a rod with a standard outer diameter. D_o was therefore chosen to be 15mm. This was used as outer diameter for all test samples. For the high pressure testing samples, an L/D ratio of 10 was chosen, and for the axial compression testing, an L/D ratio of 1.33. This means that the sample lengths were 150mm and 20mm.

2.1.2 Pressure capacity, external

During well intervention operations the CFRP tube will be subjected to an external pressure from the well. The required pressure capacity for the tube is set to 100MPa=1000bar, which is known to be one of the highest well pressures.

The high pressure testing needed to reach the failure pressure of the samples to be successful. This means that the tests were only successful if the samples failed. The high pressure pump used during the experimental testing was capable of pressures up to 20000psi (137.89MPa), so the samples had to fail before that point. 100MPa was used as P_e during the numerical analysis.

2.1.3 Submerged weight

The friction in the horizontal parts of the well is caused by the rod butting against the bottom of the casing due to the high submerged weight. The three scenarios in Figure 2-2 show how the rod/tube is behaving in the casing. This is a rough estimate, as different flows in the casing are possible.

Crude oil

Water

Mud
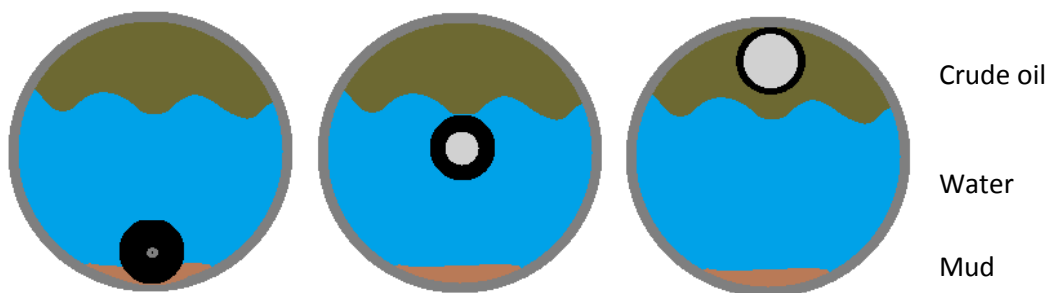
Figure 2-2: Weight scenarios

The first scenario in Figure 2-2 shows the current solid rod butting against the bottom of the tube. The second scenario is the most ideal where the tube floats in the water, but sinks in the crude oil. The third scenario shows what will happen if the submerged weight is reduced too much. The outcome will be friction against the top of the casing.

The submerged weights for a CFRP tube with a constant outer diameter of 15mm were calculated using equation 2-1 [4].

$$\left(\frac{D_o^2 - D_i^2}{4}\right)\pi\rho_{CFRP} - \frac{D_o^2}{4}\pi\rho_{fluid} + 15\,g/m \qquad \textbf{2-1}$$

Crude oil is assumed to have a density of 815 kg/m³ [5], and water has a density of 1000 kg/m³. CFRP is assumed to have a density of 1600 kg/m³ and the fiber optics implemented for sensing weighs approximately 15 g/m.

The submerged weights are calculated with equation 2-1 and shown in Figure 2-3.
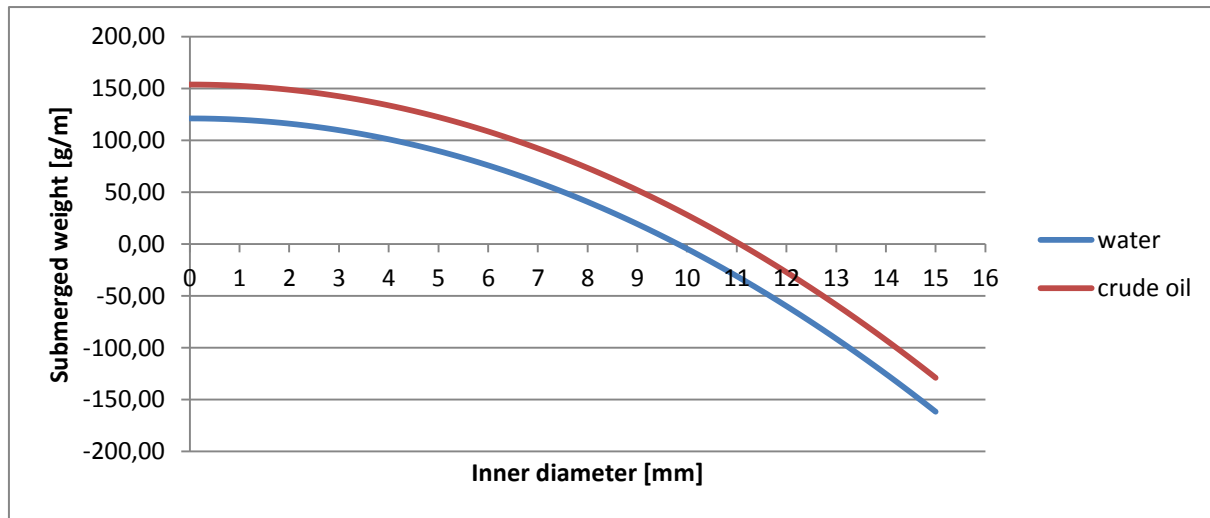
Figure 2-3: Submerged weights

Figure 2-3 shows that the tube needs an inner diameter of approximately 10mm (9.81mm) in order to behave as in the ideal scenario of Figure 2-2.

Due to the limited capacity of the high pressure pump, 12mm was used as D_i for the test samples (t = 1.5mm) to ensure successful experimental results. The submerged weight criterion was later used as guidance towards an idealized design for well intervention.

2.1.4 Bending stiffness

Existing rods are stored on drums on topside, typically with a diameter of 4200mm. This means that for well intervention, the rod not only needs to have a great pressure capacity, but also a bending stiffness that allows the tube to be spooled on the drum. The bending stress is given by equation 2-2.

$$\sigma = E\frac{r}{R} \qquad \textbf{2-2}$$
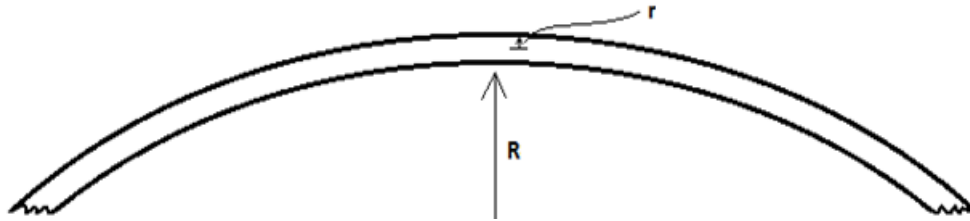
Figure 2-4: Bending stiffness

For a pure hoop wound tube where E_2 is 8000 MPa, the maximum bending stress is calculated to be $\sigma = E_2 \frac{r}{R} = 30 MPa$. The governing failure will be the transverse tensile strength (= 50MPa). Taken in account for safety factors and varying transverse tensile strength it can be concluded that pure hoop is useless for this use. To obtain a higher bending stiffness, longitudinal fibers are needed.

By comparison the bending stress with longitudinal fibers with E_1 = 140000MPa is calculated 499,8MPa. The compression strength of the fibers (=1000MPa) will govern the failure. By combining hoop and axial fibers, the tube will be more suited to withstand both the external pressure and the drum storage.

The bending stiffness is general k=EI, but for a laminate with different moments of inertia in the layers it is a bit more complex. The bending stiffness is given by $k = EI$ but since there are two layers it becomes

$$k = \sum_{n=1}^{2} E_n I_n \qquad \text{2-3}$$

where I_n is the second moment of area for a cylinder, which is shown in equation 2-4:

$$I = \frac{\pi}{64} \left(D_o^4 - D_i^4 \right) \qquad \text{2-4}$$

From equation 2-3 and 2-4 it can be found that the bending stiffness increases with higher wall thickness. It will also increase with additional fibers in the axial direction on the outermost wall of the tube. As the submerged weight and the bending stress calculated above shows, a greater wall thickness is desired, thus will the bending stiffness increase. To obtain the stiffness of the solid rod, the outer diameter of the hollow rod will necessarily have to increase.

A complete bending test was beyond the scope of this task, but the criterion of bending stiffness led to the wish to include an analysis of a composite layup that included fibers aligned in the longitudinal direction of the tube.

2.2 Manufacturing method

When manufacturing a composite material, two ingredient materials make the final product. These ingredients involve the matrix and fiber materials. When producing composite materials, the production method requires the following to ensure a desired result [6]:

- The bonding between fiber and matrix must be good
- Fiber orientation control
- Uniform distribution of fibers within the matrix
- Curing or solidification of the resin control
- Limited amount of voids and defects
- Dimensioning control for final part

A manufacturing method for the CFRP samples that fulfilled the requirements listed was essential. In addition, the choice of manufacturing method also had to have a practical approach with regard to the desired geometry and availability. A common used production method for CFRP pressure vessels and pipes is filament winding. This technique was used for the production of the CFRP samples due to its fulfillment of the above requirements, practicality and availability. This method is presented in the following section.

2.2.1 Composite filament winding

During a general filament winding process, a structural form is shaped on a rotating mandrel by winding continuous fiber around it. The fibers are accurately positioned on the mandrel in a prearranged pattern by a synchronized movement in the rotational axis of the mandrel and in variable amount of axis of the carriage. This movement spreads the fibers on the surface of the mandrel, and fully covers it after a programmed number of repetitions. By repeating the program, the process will build the thickness of the structure. Figure 2-5 illustrates the general concept of a filament winding machine [7].
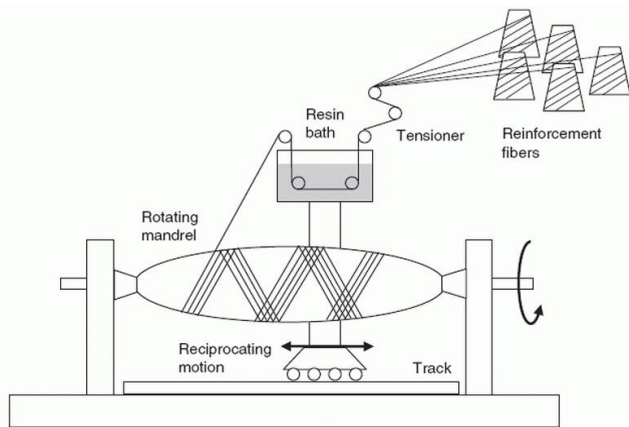
Figure 2-5: Filament winding

The fibers are initially placed on creels which obtain the tension of the fibers. This tension controls the desired fiber volume fraction and void content.

The fibers are then led through a resin bath, where the fibers are impregnated with the matrix. In the resin bath, the fibers are led by a reel that uses the tension in the fibers to thoroughly impregnate the fibers. The fibers are impregnated this way to ensure good fiber/matrix bonding and consistency of impregnation along the length. Together with the creel tension, this impregnation method also ensures that there is uniform distribution of fibers within the matrix. Then the wet fibers go through a fiber feed and placed on the mandrel.

Filament winding can be used for applications where the structure is revolved around one axis, with various shapes of the mandrel. Depending on the available motional axis, and their degrees of freedom, different winding patterns can be obtained. These are: polar, helical, circuit and pattern, layer, hoop, longitudinal and combination [8]. The method provides good fiber orientation and dimensioning control.

The main advantages for using the filament winding process is the precision in fiber placement and its repetitive qualities. Since it also uses continuous fibers and can be programmed to work automatically, the labor is relatively low. It has also the capacity of winding structures with diameters varying from a few centimeters to one or two meters.

The biggest concerns with this production method are that the mandrel must be removed afterwards. If the structure is complex and nonuniform, the mandrel must be made from a dissolvable material, or remain as a liner of the structure. Otherwise, the mandrel must be processed so that it can be removed. Another concern is that the surface quality of the finished product is often low.

2.3   Material properties and composite layups

The carbon fibers used in this work was continuous T700SC 12K ud-carbon fiber with the properties listed in Table 2-1. The resin was a mix between Araldite LY 564 and Hardener HY 2957. This mix has the properties also listed in Table 2-1. Complete material data for the carbon fibers and the epoxy are shown in Appendix A and Appendix B.

Properties for T700SC		Properties for Araldite LY 564	
$E_{1f,}\,E_{\parallel f}$	230000 MPa	E_m	2500 MPa
E_2	13333 MPa	v_m	0.35
v_{12}	0.3		
v_{13}	0.3		
v_{23}	0.55		
G_{12}	4000 MPa		
G_{13}	4000 MPa		
G_{23}	2581 MPa		
ρ	1600 kg/m^3		

Table 2-1: Fiber and epoxy data

The composite material needed to be cured at two stages, according to the resin-data. The first stage was for two hours at 60 degrees Celsius. The second stage was at 140 degrees Celsius for two hours.

Approximated material properties for the finished CFRP material are listed in Table 2-2.

E_1	140000 MPa
E_2, E_3	8000 MPa
v_{12}, v_{13}	0.3
v_{23}	0.55
G_{12}, G_{13}	4000 MPa
G_{23}	2581 MPa
ρ	1600 kg/m^3

Table 2-2: CFRP material properties

Table 2-2 lists estimated data for the material, these properties has been proven to be satisfactory for industrialized CFRP.

The following three principal composite layup configurations were chosen for investigation;

- $[\pm 80^o]$: A layup with the fibers aligned as close to normal to the axial direction as allowed by the production method of the samples. This layups was chosen to analyze a close to pure hoop wound tube. This layer was set to $\pm 80^o$ as an angle of 90° was not practically feasible.
- $[\pm 45^o]$: A layup with evenly distributed $\pm 45^o$ fibers.
- $[\pm 80^o, \pm 9^o]$: A split layup with near hoop wound fibers in the innermost half of the thickness and near longitudinal aligned fibers in the outermost half of the thickness of the tube.

2.4 Material failure

In the case of material failure of CFRP tubes subjected to external pressure, two types of material failure are distinguished; functional failure, where leakage of test fluid takes place but the structure still carries load, and structural failure, where the structure can no longer carry any load. Functional failure is caused by initial and generated micro cracks in the matrix of the composite layup. If these cracks run through the thickness of a laminate layer, it is considered as an inter fiber failure (IFF). Depending on the mode of fracture and the function of the structure, these cracks may be considered as tolerable damage [9]. Structural failure can be caused of both IFF or fiber failure (FF).

2.4.1 Failure criteria

A material subjected to complex loading may generate points in the material exposed to more than one stress component. Since the strength parameters for a material are calculated from unidirectional loading, a prediction of safe limits are needed to describe if combined stresses causes the material to yield or fracture [10]. Failure criteria are tools utilizing these strength parameters and typical loads found from testing to see whether the material fails or not.

Because CFRP are anisotropic, failure criteria becomes more complex than for isotropic materials. A well acknowledged failure criterion for explaining the behavior of composite materials is the Puck criterion. This criterion distinguishes between FF and IFF, and has a good estimation of the material behavior in a pure compression state.

Since the different laminas in a composite laminate material are transversely isotropic, Puck's failure theory distinguishes only between the parallel direction to the fiber ($\parallel$) and the transverse direction ($\perp$). With this notation, the following material strengths are introduced:

$R_\parallel^t$: fiber parallel tensile strength for uniaxial $\sigma_\parallel^t$ – stressing
$R_\parallel^c$: fiber parallel compressive strength for uniaxial $\sigma_\parallel^c$ – stressing
$R_\perp^t$: transverse tensile strength for uniaxial $\sigma_\perp^t$ – stressing
$R_\perp^c$: transverse compressive strength for uniaxial $\sigma_\perp^c$ – stressing
$R_{\perp\perp}$: transverse shear strength for pure $\tau_{\perp\perp}$- stressing
$R_{\perp\parallel}$: longitudinal shear strength for pure $\tau_{\perp\parallel}$- stressing

The stressings are illustrated in Figure 2-6.
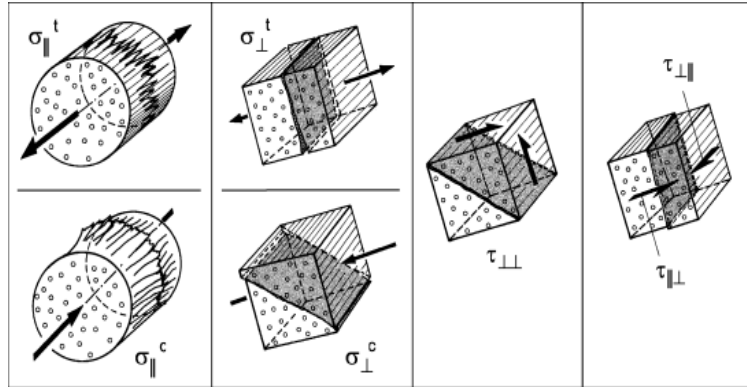
Figure 2-6: Puck's stressings

2.4.1.1 Fiber failure, FF

Puck's fiber failure criterion is based upon the common known maximum stress criterion. This theory says that fiber fracture under multiaxial stresses occurs when stresses parallel to the fiber direction in an UD-lamina is equal to or exceeds the uniaxial fiber strength of the material. This is expressed in equation 2-5 and 2-6.

$$if \ \sigma_1 \geq 0; \ f_{E,ff} = \frac{\sigma_1}{R_\parallel^t} \qquad \qquad \textbf{2-5}$$

$$if \ \sigma_1 < 0; \ f_{E,ff} = -\frac{\sigma_1}{R_\parallel^c} \qquad \qquad \textbf{2-6}$$

In equation 2-5 and 2-6, $f_{E,ff}$ is the stress exposure factor for fiber failure. General failure theory defines the relation between the stress exposure factor and failure as

$$f(\sigma, strengths) < 1 \rightarrow no \ failure$$
$$f(\sigma, strengths) = 1 \rightarrow failure \ limit$$
$$f(\sigma, strengths) > 1 \rightarrow beyond \ failure$$

Puck introduces a more sophisticated FF-condition by introducing a magnification factor $m_{\sigma f}$, which takes into account that an biaxial strain in fiber direction ε_1 between the fiber and the matrix is generated due to an uniaxial stress in the 2- or 3 direction. From this theory, the expression for the stress exposure factor can be derived. This is shown in equation 2-7 [11].

$$f_{E,FF} = \frac{1}{\pm R_\parallel^{t,c}} \left[\sigma_1 - \left(v_{\parallel\perp} - v_{\parallel\perp f} m_{\sigma f} \frac{E_\parallel}{E_{\parallel f}} \right) (\sigma_2 + \sigma_3) \right] \qquad \textbf{2-7}$$

From equation 2-7, the following relation yields:

$$R_\parallel^t \quad for \ \ [...] \geq 0$$
$$-R_\parallel^c \quad for \ \ [...] < 0$$

In equation 2-7 $v_{\parallel\perp}$ is the major Poisson's ratio for the lamina, while $v_{\parallel\perp f}$ is the major Poisson's ratio for the fiber. $E_\parallel$ is the longitudinal modulus for the lamina, wile $E_{\parallel f}$ is the longitudinal modulus for the fiber. For CFRP materials, Puck estimates the magnification factor to $m_{\sigma f} \approx 1,1$.

2.4.1.2   Inter fiber failure, IFF

This theory is very extensive and complex. Only the main topics will be introduced.

For IFF, Puck introduced the following fracture hypothesis [12]:

"Inter Fiber Fracture on a plane parallel to the fibers is caused by the stresses σ_n and $\tau_{n\psi}$ acting on the fracture plane. (...) If σ_n is a tensile stress it promotes fracture together with the shear stress $\tau_{n\psi}$ or even alone for $\tau_{n\psi} = 0$. In contrast to that σ_n impedes fracture if it is a compressive stress by raising the fracture resistance of the fracture plane against shear fracture with increasing compressive stress σ_n."

As mentioned in his fracture hypothesis, Puck has focused his IFF theory on section planes in the material. On these planes, only one normal stress $\sigma_n(\theta)$ and two shear stresses $\tau_{nt}(\theta)$ and $\tau_{n1}(\theta)$ are
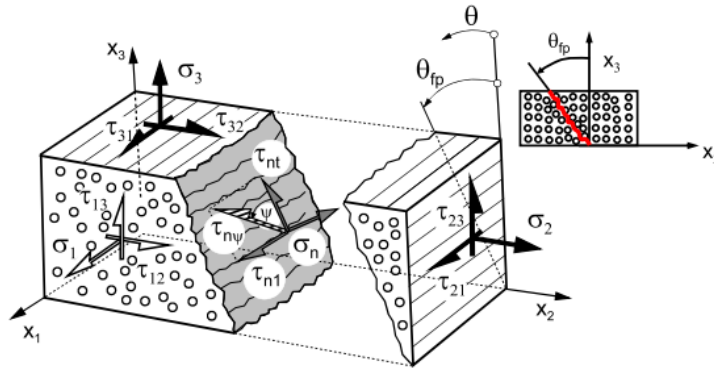
Figure 2-7: Puck's action plane

acting. If these stresses are acting on a common action plane, failure may occur in an action plane inclined with the angle Θ_{fp}. An illustration is given in Figure 2-7 [13].

The stresses are given by equation 2-8, 2-9 and 2-10.

$$\sigma_n(\theta) = \sigma_2 \cdot cos^2\theta + \sigma_3 \cdot sin^2\theta + 2 \cdot \tau_{23} \cdot sin\theta \cdot cos\theta \qquad \text{2-8}$$
$$\tau_{nt}(\theta) = -\sigma_2 \cdot sin\theta \cdot cos\theta + \sigma_3 \cdot sin\theta \cdot cos\theta + \tau_{23} \cdot (cos^2\theta - sin^2\theta) \qquad \text{2-9}$$
$$\tau_{n1}(\theta) = \tau_{31} \cdot sin\theta + \tau_{21} \cdot cos\theta \qquad \text{2-10}$$

As a consequence, Puck also introduces three fracture resistances of the action plane; $R_\perp^{At}$, $R_{\perp\perp}^A$ and $R_{\perp\parallel}^A$. The definitions are as follows;

$R_\perp^{At}$: Resistance of the action plane against its fracture due to transverse tensile stressing $\sigma_\perp^t$ acting in that plane.
$R_{\perp\perp}^A$: Resistance of the action plane against its fracture due to transverse shear stressing $\tau_{\perp\perp}$ acting in that plane.

11

$R_{\perp\parallel}^A$: Resistance of the action plane against its fracture due to longitudinal shear stressing $\tau_{\perp\parallel}$ acting in that plane.

In his analysis, Puck distinguishes between three modes of fracture. These modes will not be presented in detail, but it can be said that they are mainly distinguished by which stressings that causes fracture to occur, and how these combinations of stressings determines the fracture plane angle. To be able to calibrate the fracture curve in the transition between the different modes, Puck also presents some inclination parameters, which are found empirical. The suggested values are shown in Table 2-3 [14].

$\varphi = 60\%$	$p_{\perp\parallel}^t$ $[-]$	$p_{\perp\parallel}^c$ $[-]$	$p_{\perp\perp}^t$ $[-]$	$p_{\perp\perp}^c$ $[-]$
CFRP/epoxy	0.35	0.3	0.25-0.3	0.25-0.3

Table 2-3: Inclination parameters

The inclination parameters, together with equation 2-11, 2-12 and 2-13 keep the fracture envelopes for all combinations of stressings continuous.

$$\frac{p_{\perp\psi}^{t,c}}{R_{\perp\psi}^A} = \frac{p_{\perp\perp}^{t,c}}{R_{\perp\perp}^A} cos^2\psi + \frac{p_{\perp\parallel}^{t,c}}{R_{\perp\parallel}^A} sin^2\psi \qquad \text{2-11}$$

$$cos^2\psi = \frac{\tau_{nt}^2}{\tau_{nt}^2 + \tau_{n1}^2} \qquad \text{2-12}$$

$$sin^2\psi = 1 - cos^2\psi \qquad \text{2-13}$$

From all the relations above, the IFF stress exposure factor can be derived:

If $\sigma_n \geq 0$:

$$f_E(\theta) = \sqrt{\left[\left(\frac{1}{R_\perp^t} - \frac{p_{\perp\psi}^t}{R_{\perp\psi}^A}\right) \cdot \sigma_n(\theta)\right]^2 + \left(\frac{\tau_{nt}(\theta)}{R_{\perp\perp}^A}\right)^2 + \left(\frac{\tau_{n1}(\theta)}{R_{\perp\parallel}}\right)^2} + \frac{p_{\perp\psi}^t}{R_{\perp\psi}^A}\sigma_n(\theta) \qquad \text{2-14}$$

If $\sigma_n < 0$:

$$f_E(\theta) = \sqrt{\left(\frac{p_{\perp\psi}^c}{R_{\perp\psi}^A} \cdot \sigma_n(\theta)\right)^2 + \left(\frac{\tau_{nt}(\theta)}{R_{\perp\perp}^A}\right)^2 + \left(\frac{\tau_{n1}(\theta)}{R_{\perp\parallel}}\right)^2} + \frac{p_{\perp\psi}^c}{R_{\perp\psi}^A}\sigma_n(\theta) \qquad \text{2-15}$$

An illustration of the IFF master fracture body is shown in Figure 2-8.
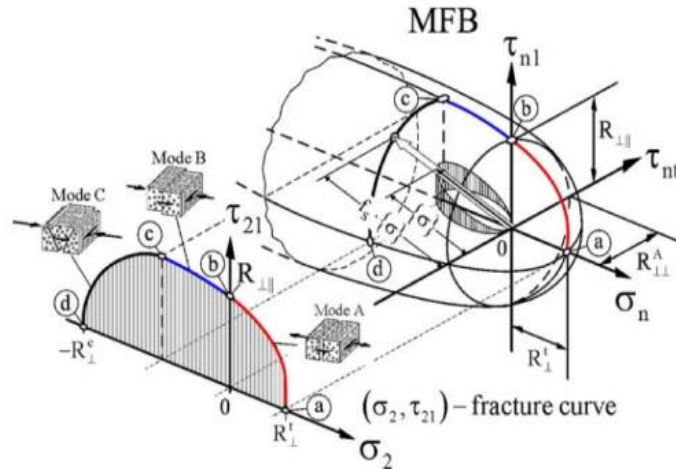
Figure 2-8: Master fracture body

2.4.1.3 Weakening

Puck states that the IFF mode is not completely independent of stresses parallel to the fibers (σ_1). This theory has many considerations, but one important factor is that $f_{E,IFF}$ is weakened by a factor $\mu_{1,W}$, a function of $f_{E,FF}$, when σ_1 passes a certain limit. This is illustrated in Figure 2-9 [15]. The weakening factor is given by equation 2-16 where f_{E1} is the adjusted stress exposure factor, and f_{E0} is the unaffected stress exposure factor. As seen from Figure 2-9, this has an effect when $f_{E,FF}$ exeeds the value of 0.6.

$$f_{E,1} = \frac{f_{E,0}}{\mu_{1,W}}$$

2-16
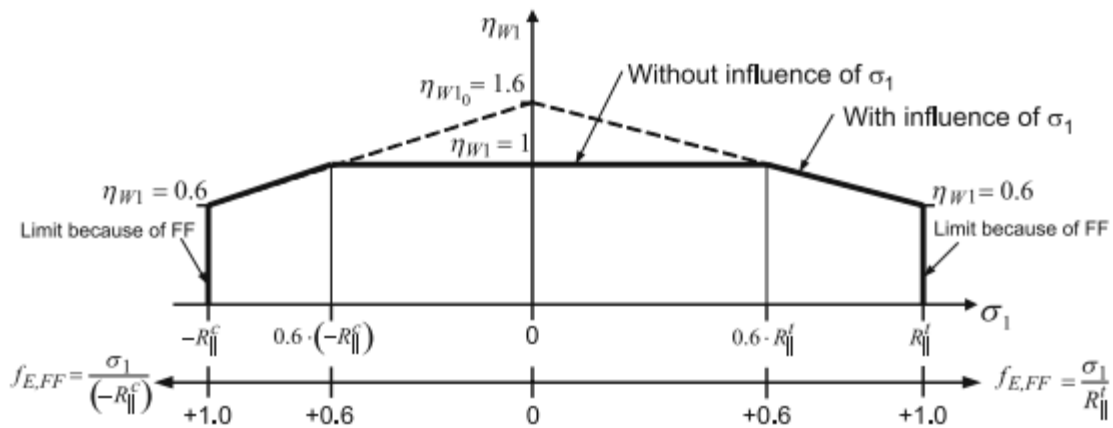
Figure 2-9: Stress exposure factor weakening

13

2.5 Buckling

Buckling is a very common failure mode for structures subjected to compressive stress. Buckling is mainly the cause when the failure happens at a critical load lower than the ultimate loads the material is capable of, and the failure is regarded as a stability problem [16]. This failure mode depends primarily on the geometry of the structure and its elastic properties.

For infinite long composite cylindrical shells and tubes subjected to external pressure, the first buckling mode will cause the tube to deform into an elliptical shape before failure. This collapse is called local buckling and occurs because the combination of the axial and radial pressure has a stabilizing effect. This is opposed to global buckling where the structure beds out from its axial axis. Buckling failure is often more dramatic than the failures seen in material failure.

The external collapse pressure of very thin isotropic cylinders is governed by classical elastic buckling formulas; however for thicker anisotropic composite tubes the theory is extensive.

The work of E. Groves and A.L. Highsmith (1994) [17] concentrated on the collapse of relatively thick (R/t = 10) and relatively short (L/D=1) composite tubes. This work shows that for a given geometry and material system, ply layup has a significant effect on the predicted buckling load and that the predicted buckling load increases with the ply angle. However, an analysis on how this affected the material failure mode was not conducted in that work. It was also shown that for a $[90^o/0^o]$ layup, the critical buckling load increased with an increased hoop/longitudinal ratio. A $[\pm45^o]$ layup was proven to have a higher critical buckling load than a hoop/longitudinal ratio of 3.

3 Finite element modeling and numerical analyses

The numerical analysis was conducted using the finite element method (FEM) with the purpose of preparing and substantiating the results obtained from the experimental testing. Puck's failure theory was implemented in the analysis to quantify and verify the material's strength properties. The numerical analysis was therefore both used as a pre-study for the experimental testing and for a post-study to validate the results to assure the reliability of the numerical models.

The goal of this analysis was to numerically analyze CFRP test samples with three different composite layups to find the ideal critical load, P_{cr}, that would cause the structure to fail. If the samples failed due to material failure, the stress combinations in the areas that governed the failures were to be localized and documented. After the physical problem was accurately defined and modeled, the stresses could be calculated in all points of the FEM model. Puck's failure theory could then use these stresses to calculate the stress exposure factor, which indicated at what ideal load the given material layup would fail. The primary parameters for evaluation were P_{cr} and the elastic and strength properties of the material. With these results, an optimized layup could be evaluated.

Computer aided engineering, CAE, was used for the numerical analysis. With this method, digital three dimensional FEM models of the CFRP samples could be modeled and analyzed. All the modeling and analysis was done with the FEM software *Abaqus/CAE 6.11*.

3.1 Numerical model for high pressure testing

Three FEM models were created for the high pressure simulation where each model was analyzed for linear static stress and for an eigenvalue buckling analysis. All models had the same geometry, but different composite layup properties. The same modeling procedure was thus mostly applicable for all three models.

3.1.1 Geometry and model

The FEM model had to respond to the subjected pressure as similar to the CFRP test samples as possible for achieving a successful numerical analysis. During the high pressure testing, the CFRP test samples were in direct contact with other components. This made an impact on the results, and had to be included to the numerical model. These relations are illustrated in Figure 3-1. As seen in Figure 3-1, two components were in direct contact with the CFRP samples; the lid and the plug.
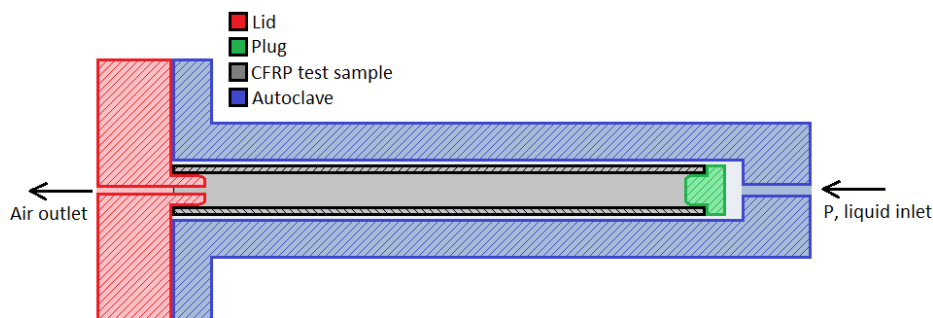
Figure 3-1: Interacting components

Due to the composite properties of the tube, and since the stresses due to the external pressure was nonlinear through the tube thickness; both an axisymmetric model and a shell element analysis would be inadequate for this analysis. A full 3D stress analysis was thus necessary for the whole model to be accurately modeled, and the tube had to be modeled as a solid with composite layup.

The parts were modeled according to the dimensions of the existing equipment. The parts were modeled by revolving a base sketch 360° around the same axis since all parts were cylindrical shaped. To avoid distortion of the mesh a hole was included in the plug. The thickness of the lid was reduced to 10mm to remove redundant elements in the mesh. These changes had no influence on the results. The base sketches with dimensions are shown in Figure 3-2 (top left: the lid, top right: the plug, bottom: the tube). The green lines in Figure 3-2 are the axis of revolution. Dimensions are in millimeter.
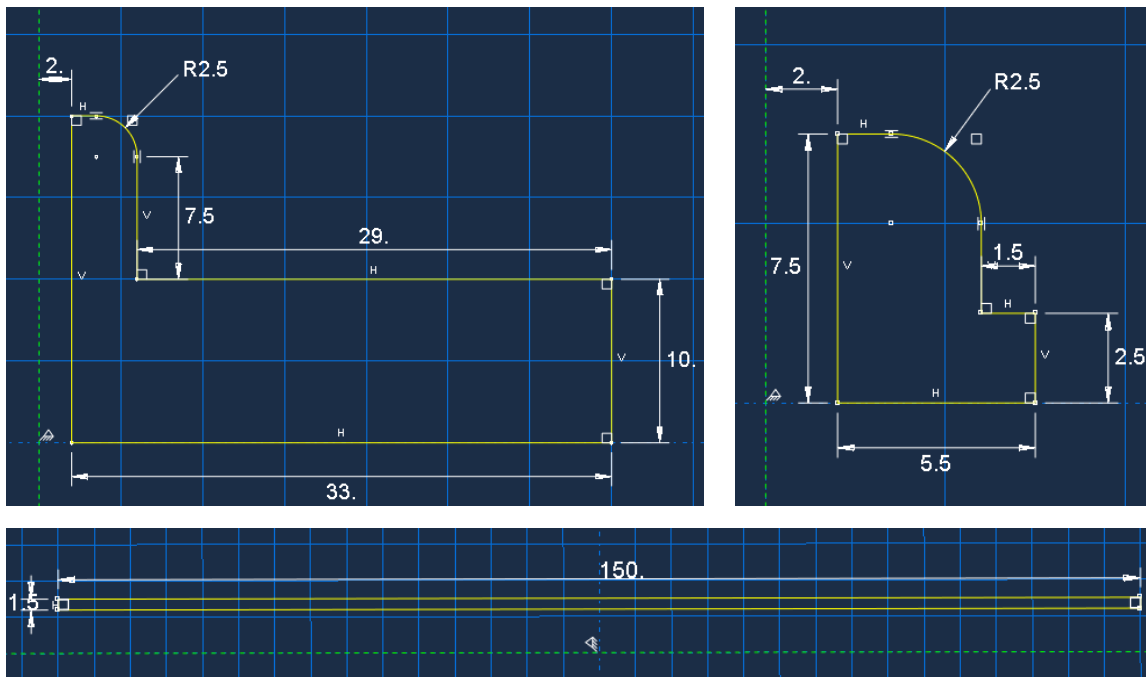
Figure 3-2: Base sketches of the parts

For meshing and interaction control, and to facilitate forthcoming tasks, the parts were partitioned into smaller cells. The results of the partitioning operations are shown in Figure 3-3.

Lid: 24 cells   Tube: 12 cells   Plug: 20 cells
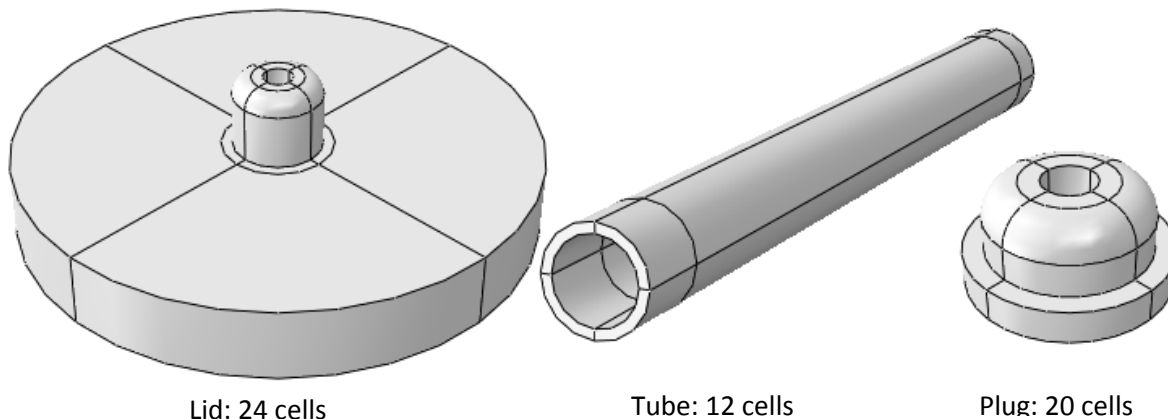
Figure 3-3: Revolved and partitioned parts

16

A wire framed illustration of the finished assembly is shown in Figure 3-4.
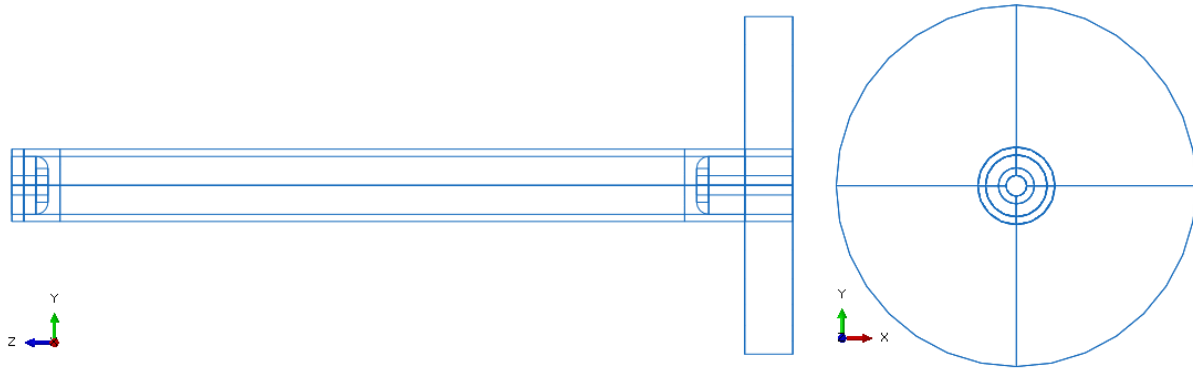
Figure 3-4: Assembly

3.1.2 Analysis procedures

For the buckling analysis, a linear perturbation buckling procedure was used. As opposed to an analysis based on RIKS method, this method does not introduce a material imperfection, and can be considered as an ideal model. This was found to be sufficient for this thesis. Four eigenvalues were requested, and an adequate maximum number of iterations were used for the analysis to complete.

For the static stress analysis, a *Static, general* load step was created. The nlgeom setting was turned on, which made Abaqus account for geometric nonlinearity in the calculations. An adequate maximum number of iterations were also used in this load step for the analysis to complete.

3.1.3 Loads and boundary conditions

Due to linear-elastic theory, any input load to the model would generate the same failure load prediction if the model remained unchanged. The input load, the uniformly distributed external pressure P_e, could therefore be randomly chosen. P_e was chosen to 100MPa, according to the design criteria mentioned in section 2.1.2. The critical failure pressure, P_{cr}, was either the failure load predicted by Puck's failure criterion, whether it predicts failure due to FF or IFF, or the load that made the structure buckle. P_{cr} was the most important output of the numerical analysis. A uniform pressure of 100MPa was thus subjected to the model in the load step on the surfaces shown in Figure 3-5. To compensate for the hole in the plug, the subjected pressure in the axial direction was increased to 107.66MPa according to equation 3-1. The back faces of the lid were encastred in the initial step of the analysis.

$$\frac{P_i \cdot \pi \cdot {d_o}^2}{\pi \cdot ({d_o}^2 - {d_i}^2)} = \frac{100MPa \cdot \pi \cdot 7.5mm^2}{\pi \cdot (7.5mm^2 - 2mm^2)} \qquad \text{3-1}$$
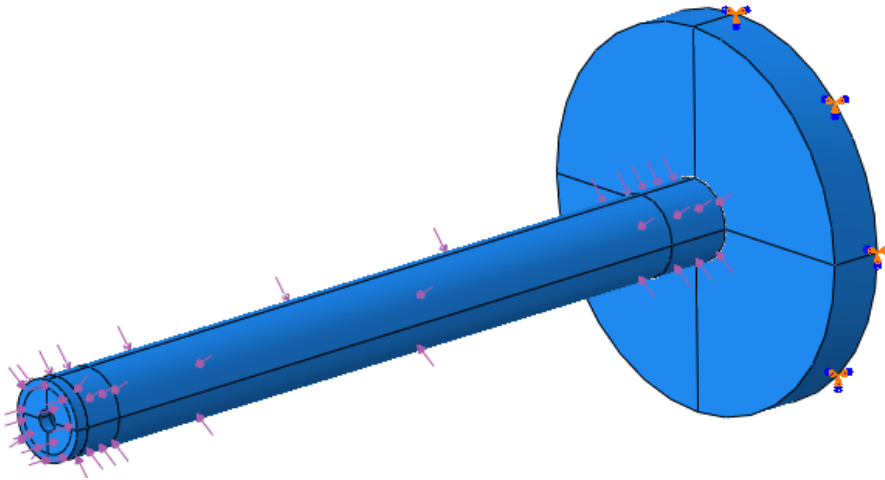
Figure 3-5: Loaded and fixed assembly

3.1.4 Element types and meshing

The element types and the meshing technique had to provide results with as low percent of error as possible. Abaqus has a large library of element types, which enables a customized choice of element types for the proper usage.

For a thick-walled composite tube subjected to uniform external or internal pressure, lowest error is obtained with several 20-node quadratic brick elements with reduced integration (C3D20R) elements in the radial direction [18]. These are second-order continuum elements which capture stress concentrations more effectively, and model a curved surface with fewer elements than first-order elements. They are also very effective in bending-dominated problems [19]. This element type was therefore a suitable choice for the tube. Reduced integration generally yield more accurate results and reduces the running time of the analysis.

The generated stresses in the lid and the plug were not to be analyzed. The element type for these parts was thus chosen due to computational efficiency instead of performance. 8-node linear brick elements with reduced integration and hourglass control (C3D8R) were chosen since they had fewer nodes and it was a sufficient choice regarding performance.

The following requirements influenced the choices of how the mesh was structured:

- The ends of the tube were the critical areas of the finite element model. The plug and the lid would oppose to the tube's natural response to the external pressure and accumulate local stress concentrations around the contact surfaces. To avoid large variation of stress within each element, a refinement of the mesh was necessary to increase the convergence rate and obtain a more accurate result. This was done in the axial direction of the tube by seeding cells at the ends with higher concentration of elements, while allowing a coarser mesh in the middle section of the tube.
- To find the location of the governing failure, elements had to be evenly distributed throughout the tube (in accordance with the stress concentration). Only in this way could the subscript of

Puck's failure criterion find the precise location of the elements with the highest exposure factor. This meant that there had to be more than one element through the thickness of the tube wall.

- To evenly distribute the plies of the composite layup, the number of elements in the radial direction of the tube had to be constant. Four elements were chosen through the thickness of the tube (radial direction).
- To prevent overclosures and element penetrations, and for computational efficiency for the interaction settings, the contact pair surfaces were meshed equally.
- Insignificant and noncritical areas in the model were meshed with large elements for computational efficiency.

In order to fulfill the meshing requirements, the following edges were seeded by number with a constraint so that the number of elements was not allowed to change:

- All edges in the radial direction of the tube and their opposing edges of the plug and lid were seeded with *4* elements.
- All edges in the circumferential direction of all parts, except from the outermost circular edges of the tips of the plug and lid, were seeded with *15* elements, which gave a total of 60 elements in the circumference.
- Edges *(a), (c), (d)* and *(e)* in Figure 3-6 were seeded with *12*, *20, 12* and *4* elements, respectively.
- Edge *(b)* in Figure 3-6 was seeded by size with a double bias, controlled with a minimum size of 2.6 and a maximum size of 20.
- The remaining edges of the plug and lid were seeded so that the mesh was generated to be satisfactory with as few elements as possible.
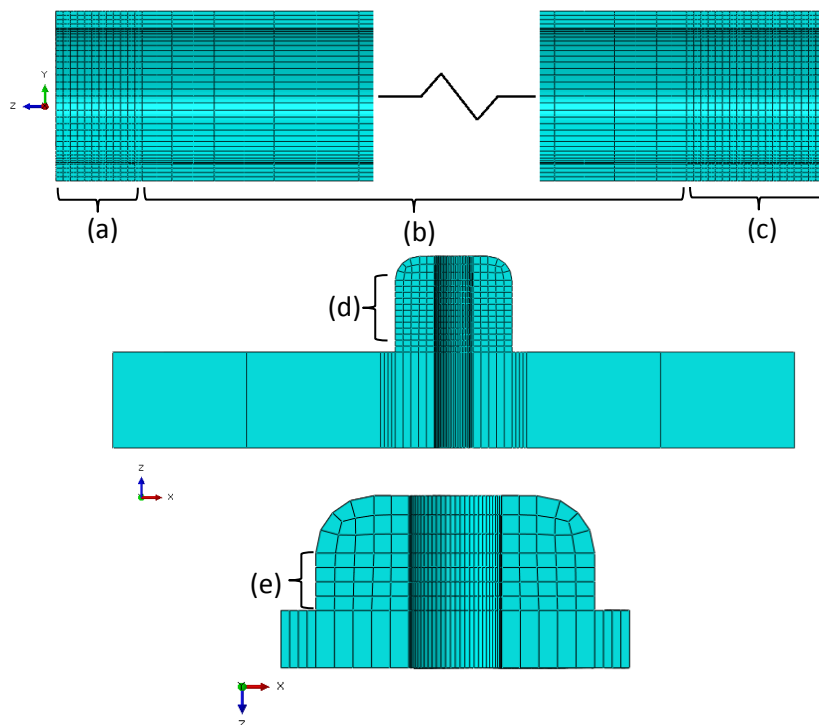
Figure 3-6: Edge seeding. From top: Tube, lid and plug

Since all the parts were revolved around the same axis, a swept meshing technique was an obvious choice. This technique gave controlled meshing with the *Medial Axis* algorithm, which minimized the mesh transition. This function helped to reduce the mesh distortion.

The tube was assigned a stack direction with the *Assign Stack Direction* option. One of the curved faces on the outside of the tube was chosen as reference orientation.

The meshing generated 10040 elements on the tube, 5780 elements on the lid and 2580 elements on the plug. The fully meshed parts are shown in Figure 3-7.
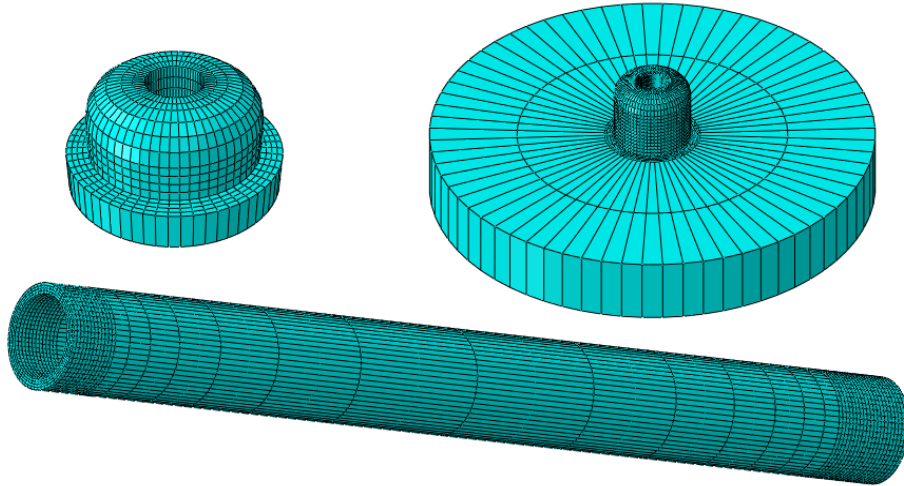
Figure 3-7: Fully meshed parts

3.1.5 Properties

The lid and the plug were made of steel, whilst the tube was made of CFRP. These materials were defined in Abaqus. The material properties used for CFRP is listed and discussed in Section 2.3. The material properties used for the steel was the same as for conventional steel [20]. These properties are shown in Appendix C. The material was assigned to the plug and the lid by creating and assigning them a solid, homogenous section.

Different composite layup was created for each model. These layups are described in section 2.3. They were all assigned a ply count of 8 (two for each elements through the thickness), which was found to be adequate.

Due to the geometry of the test samples, a cylindrical coordinate system was used. In general composite theory, the designated axis in a global Cartesian coordinate system are x, y and z and x_1, x_2 and x_3 for the local (material) coordinate system. For the global coordinate system, the x axis is the axis parallel to the fiber direction, the y axis is the axis normal to the fibers in the laminate plane, and the z axis is the axis normal to the laminate plane of the fibers. In the material coordinate system these directions are designated as x_1, x_2 and x_3 respectively. Angel α is the angle between axis x and x_1 [21].

The notations for the cylindrical coordinate system is (z,θ,R), which in this thesis represented the Cartesian (x,y,z) coordinates respectively. Regarding the production method for the samples, the z axis was chosen as the primary axis, since filament winding uses the axial direction as a reference for the fiber direction. The θ axis represents the tangential direction of the samples and the R axis represents the radial direction. An illustration of the orientations is shown in Figure 3-8.
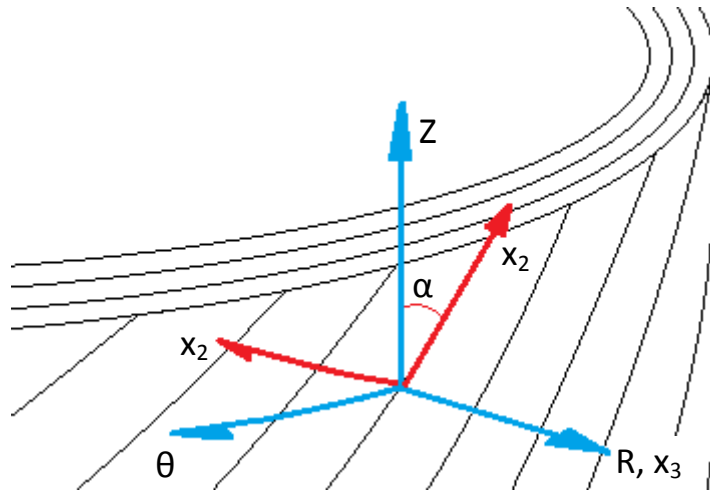
Figure 3-8: Material orientations

To be able to be consistent about stress notations, the definitions listed in Table 3-1 were used:

	Stress in axial direction	Stress in tangential direction	Stress in radial direction	Shear stress
Global CSYS (z,θ,R)	σ_z	σ_θ	σ_R	$\tau_{z\theta}$
Material CSYS (x_1,x_2,x_3)	σ_1	σ_2	σ_3	τ_{12}

Table 3-1: Material orientations

A discrete definition was used for layup orientation, and the axis was chosen according to the discussion above. The rotation axis was axis 3, and no additional rotation was chosen. Element direction 3 (the radial direction) was chosen as the stacking direction.

To be able to efficiently define regions for the plies in the composite layup, four element s*ets* on the tube were needed to be created. These are shown in Figure 3-9.

Region1   Region2   Region3   Region4
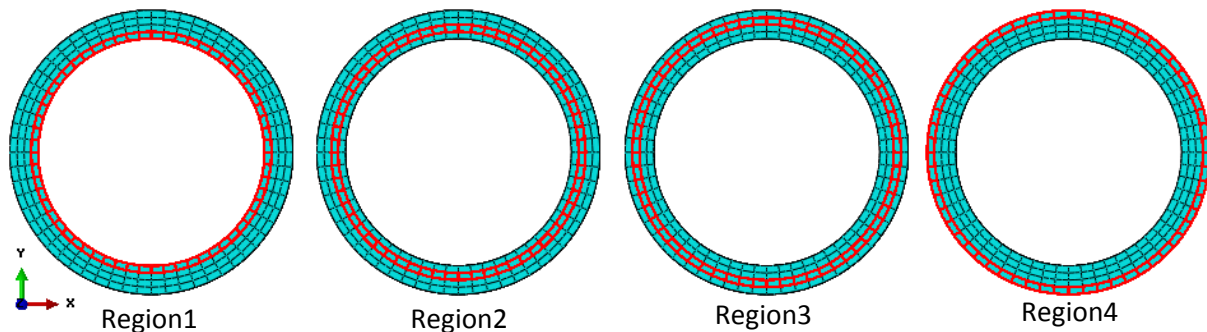
Figure 3-9: Defined regions for the composite plies

The Abaqus documentation states that "*If the region to which you assign your solid composite layup contains multiple elements, each element will contain the plies defined in the ply table, and the analysis results will not be as expected.*" [22]. Due to this, each ply was applied to each corresponding native mesh element set in the stacking direction. Ply 1 and 2 was thus given to the innermost layer of elements of the tube (*Region1*), ply 3 and 4 was given to the second layer of elements of the tube (*Region2*) etc. This allowed each ply to be separately analyzed in the results-section.

Since the Abaqus documentation also states that "*The actual thickness of a ply is the element thickness times the fraction of the total thickness that is accounted for by each ply*" [23], the Element Relative Thickness was set to 1. Three section integration points was specified in each layer. Since the analysis was linear elastic, this was sufficient to describe the stress distributions through the section.

The final laminate stacking sequences for the FEM models were $[\pm80°]_4$, $[\pm45°]_4$ and $[\pm80°_2, \pm9°_2]$

There was no need for assigning the plug and the lid a material orientation, since these parts were not to be analyzed.

3.1.6   Interactions and contacts; assumptions and configurations

In the experimental testing, both the lid and the plug were glued on to the test samples with strong epoxy glue. This was done both to keep the parts together and to seal the gap for preventing leakage. The glued surfaces in one end of the tube are highlighted in Figure 3-10. During the high pressure testing it was assumed that there was relative movement between the glued surfaces colored in red in Figure 3-10. Since there was no leakage in the system during the test, it was also assumed that the green surfaces in Figure 3-10 had no relative movement and was still tied together by the glue. These assumptions were implemented in the model by the use of two *interactions* and two *constraints*.
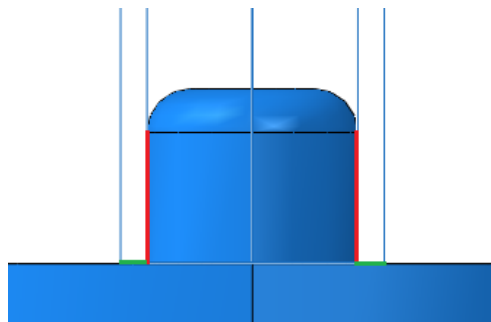
Figure 3-10: Interacting surfaces in one of the two ends

The interactions were defined for the surfaces in contact in the Z-θ plane (colored in red in Figure 3-10) at both the lid-end and the plug-end. Properties for the contact were defined both in the tangential- and the normal direction. For the tangential behavior, a penalty friction formulation was chosen. It was assumed that the friction was pretty rough due to the glue, thus the friction coefficient was set to *0.6*. For the normal behavior, a "hard" pressure-overclosure contact type was chosen with penalty as the constraint enforcement method. The stiffness scale factor was adjusted to *100* to obtain a stiff contact between the surfaces.

General contact was chosen as contact formulation for the interactions. This formulation uses the surface-to-surface contact discretization, which is generally more accurate than the node-to-surface method. General contact also uses the finite-sliding tracking approach. Since the tube would have a relatively larger deformation, and thus a greater relative elemental movement than the plug and lid, finite sliding was best suited for this application. This approach is also best suited than the other contact formulations for modeling contact near corners.

General contact automatically assigns the master and slave roles to surfaces. The surfaces selected for general contact were surface *(a), (b), (c)* and *(d)* in Figure 3-11.

(a) (b) (c) (d)

(e) (f) (g) (h)
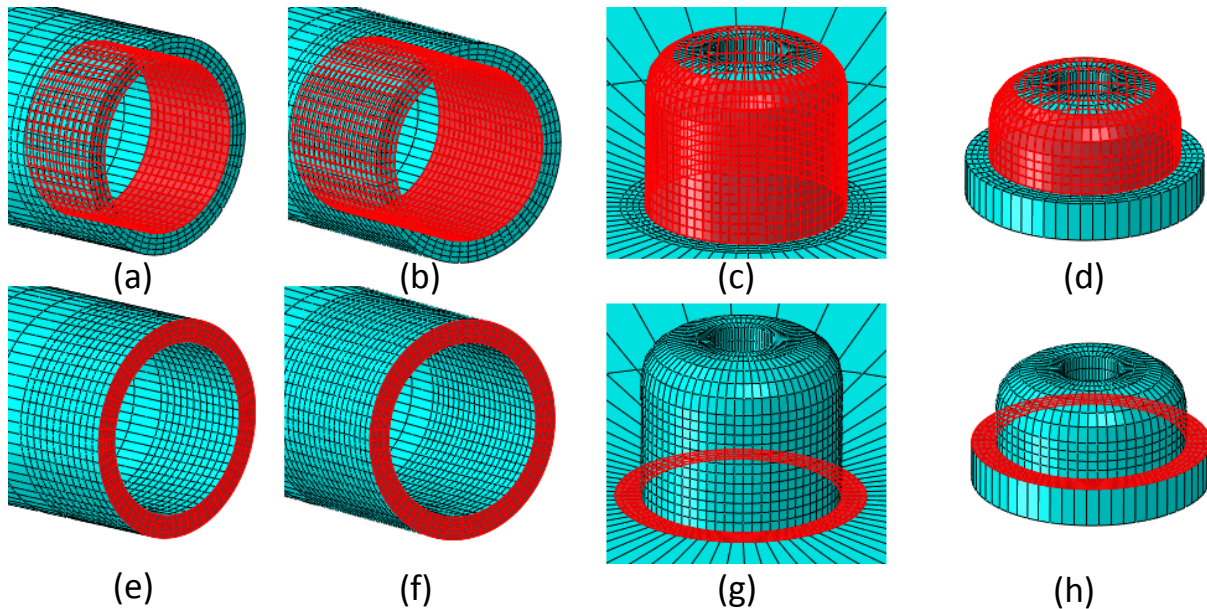
Figure 3-11: Contact surfaces

The constraints were two ties where surface *(e)* and *(f)* in Figure 3-11 were assigned the role as master surface, while surface *(g)* and *(h)* were assigned the role as slave surface. The discretization method was surface-to-surface, and *0.1* was set as position tolerance.

3.2 Numerical model for axial compression testing

Three standard FEM models were created for the axial compression testing; one for each composite layup configuration. These models were all analyzed for linear static stress and for eigenvalue buckling.

The discussions and operations conducted in section 3.1.2: *analysis procedures* and section 3.1.5: *properties* for the high pressure testing models yielded also for the axial compression models, and were thus excluded in this section.

3.2.1 Geometry and model

From the experimental testing, it could be seen that the axial compression samples deformed into a barrel shape. This was due to that the friction between the test samples and the plates retarded the motion of an expanding diameter of the samples. It was desirable to include this effect in the numerical model. One simple way of doing so is to make a kinematic coupling between one of the tube edge

surfaces to a control point on the axial axis. This constraint counteracts the Poisson effect of that surface, and obtains its initial shape. For this function to work properly, the whole tube had to be modeled. This stands in contrast to the common reasoning about creating an axisymmetric model, but the computational cost was considered low, hence the trade-off was satisfactory.

The tubes were modeled according to the dimensions of the experimental test samples, whose dimensions are listed in Table 3-2. For efficiency, the length was chosen to be *20mm* for all FEM models.

Sample #	Length [mm]	Inner diameter [mm]	Outer diameter [mm]	Cross section area [mm^2]	Layup
1	19,45	12,00	15,15	67,17	$[\pm45]_n$
2	20,25	12,00	15,15	67,17	$[\pm45]_n$
3	20,05	12,00	15,15	67,17	$[\pm45]_n$
4	20,65	12,00	15,15	67,17	$[\pm45]_n$
5	21,00	12,00	15,55	76,81	$[(\pm80)_{n/2}/(\pm9)_{n/2}]$
6	19,00	12,00	15,55	76,81	$[(\pm80)_{n/2}/(\pm9)_{n/2}]$
7	19,60	12,00	15,55	76,81	$[(\pm80)_{n/2}/(\pm9)_{n/2}]$
8	19,70	12,00	15,55	76,81	$[(\pm80)_{n/2}/(\pm9)_{n/2}]$
x	20,00	12,00	15,00	63,61	$[\pm80]_n$

Table 3-2: Sample numbering and dimensions

3.2.2 Loads and boundary conditions

To evenly distribute the loading force, a kinematic coupling was created. One of the end surfaces of the tube was picked as the surface for the coupling, and a reference point in the circumference center of the same plane was picked as control point. All of the degrees of freedom for this coupling were constrained.

The load was then set as a concentrated force in the reference point with a direction negative to the axial direction. The magnitude of the force was given by equation 3-2. P_e was set to 100MPa.

$$F = \pi(R_o{}^2 - R_i{}^2) * P_e \qquad \qquad \text{3-2}$$

The bottom surface of the tube was encastred in all directions. The load, constrains and the coupling are shown in Figure 3-12.
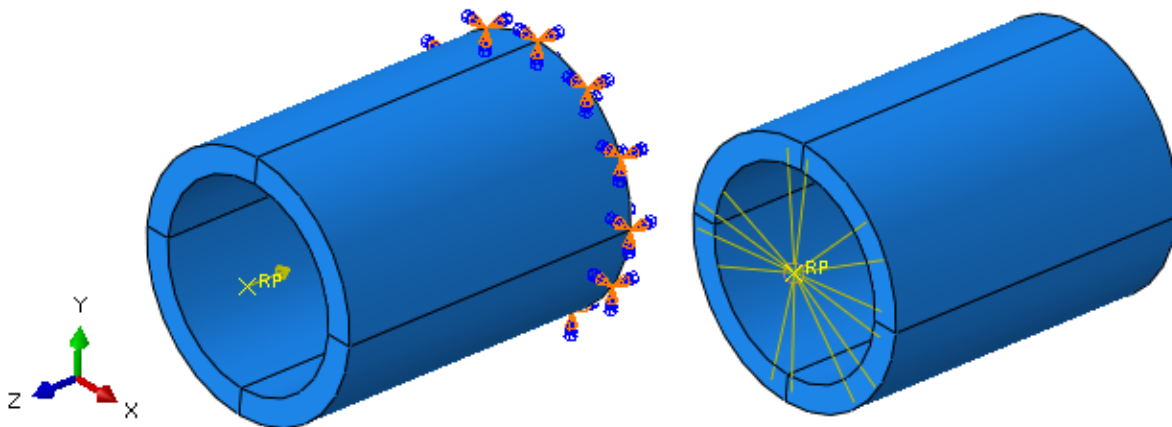
Figure 3-12: Loads and boundary conditions

24

3.2.3 Element types and meshing

The tube was given four elements in the radial direction and sixty elements in the tangential direction. A structural meshing technique generated 3600 elements on the model, which is shown in Figure 3-13. C3D20R elements were also used for this tube.
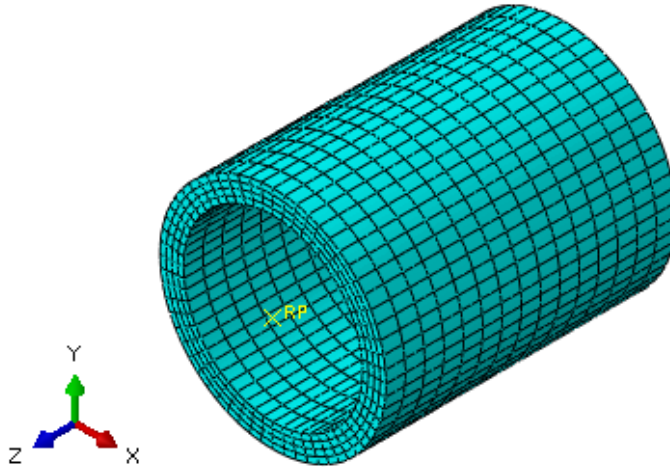
Figure 3-13: Fully meshed model

3.3 Implementation of Puck's failure criterion

For numerical efficiency, Puck's failure criterion was implemented with Abaqus CAE software by running a python script after the analysis of the model was done.

The script calculated the fracture plane angles and stress exposure factor values for both FF and IFF for a predefined region of the model and wrote these values as an output. It also found the stress exposure factor for the Max Stress failure criterion. The location of the critical elements was indicated with a color scale.

The following material properties and strength parameters were initially used in the script is listed in Table 3-3. The chosen strength values are achievable for a typical industrial composite.

Elastic and strength properties:		
E_1	140 000	
E_2	8 000	
v_{12}	0.30	Major poissons number
v_{23}	0.55	
G_{12}	4 000	
F_1^t	1 500	Longitudinal tensile strength (=$R_\parallel^t$)
F_1^c	1 000	Longitudinal compressive strength (=$R_\parallel^c$)
F_2^t	50	Transverse tensile strength (=$R_\perp^t$)
F_2^c	150	Transverse compressive strength (=$R_\perp^c$)
F_{12}	75	Longitudinal shear strength (=$R_{\perp\parallel}$)
F_{23}	50	Transverse shear strength (=$R_{\perp\perp} = R_{\perp\perp}^A$)
Parameters used in Puck's failure criterion		
E_1^f	230 000	Longitudinal fiber modulus
v_{12}^f	0.20	Major poissons number of fiber
$m_{\sigma f}$	1.1	Multiplication factor (recommended CFRP=1.1)
$p_{\perp\parallel}^t$	0.35	IFF inclination factor (0.35 recommended)
$p_{\perp\parallel}^c$	0.30	IFF inclination factor (0.30 recommended)
$p_{\perp\perp}^t$	0.25	IFF inclination factor (0.25-0.30 recommended)
$p_{\perp\perp}^c$	0.25	IFF inclination factor (0.25-0.30 recommended)

Table 3-3: Parameters used in Puck's failure criterion

When the stress exposure was calculated, the predicated failure stress could be found by equation 3-3.

$$P_{cr} = \frac{P_e}{f_E} \qquad \text{3-3}$$

3.4 Numerical results for high pressure models

3.4.1 Model verification

For an isotropic thick walled cylinder subjected to external pressure, the stresses in the axial, tangential and radial direction can be calculated by equations 3-4, 3-5 and 3-6 [24].

$$\sigma_{R,ISO} = -\frac{1-\left(\frac{R_i}{R}\right)^2}{1-\left(\frac{R_i}{R_o}\right)^2} P_e \qquad \text{3-4}$$

$$\sigma_{\theta,ISO} = -\frac{1+\left(\frac{R_i}{R}\right)^2}{1-\left(\frac{R_i}{R_o}\right)^2} P_e \qquad \text{3-5}$$

$$\sigma_{z,ISO} = -\frac{1}{1-\left(\frac{R_i}{R_o}\right)^2} P_e \qquad \text{3-6}$$

In equations 3-4, 3-5 and 3-6, R is the variable radius, spanning from R_i to R_o. Calculating these equations gives the results given in Figure 3-14. The same stress components were plotted from the [±45°] and the [±80°] FEM model results, which are also shown in Figure 3-14.

Stress components through the thickness

Legend:
- σ3,±45 = 15,021R^2 - 268,49R + 1068,8
- σ2,±45 = 3,7061R^2 - 72,579R + 240,65
- σ1,±45 = -57,566R^2 + 939,4R - 4394,3
- σ1,±80 = -99,544R^2 + 1574,4R - 6581,5
- σ2,±80 = 12,488R^2 - 199,59R + 521,71
- σ3,±80 = 25,356R^2 - 407,02R + 1527
- σR,isotropic = 14,726R^2 - 264,88R + 1058,6
- σθ,isotropic = -14,726R^2 + 264,88R - 1614,2
- σz,isotropic = - 277,78
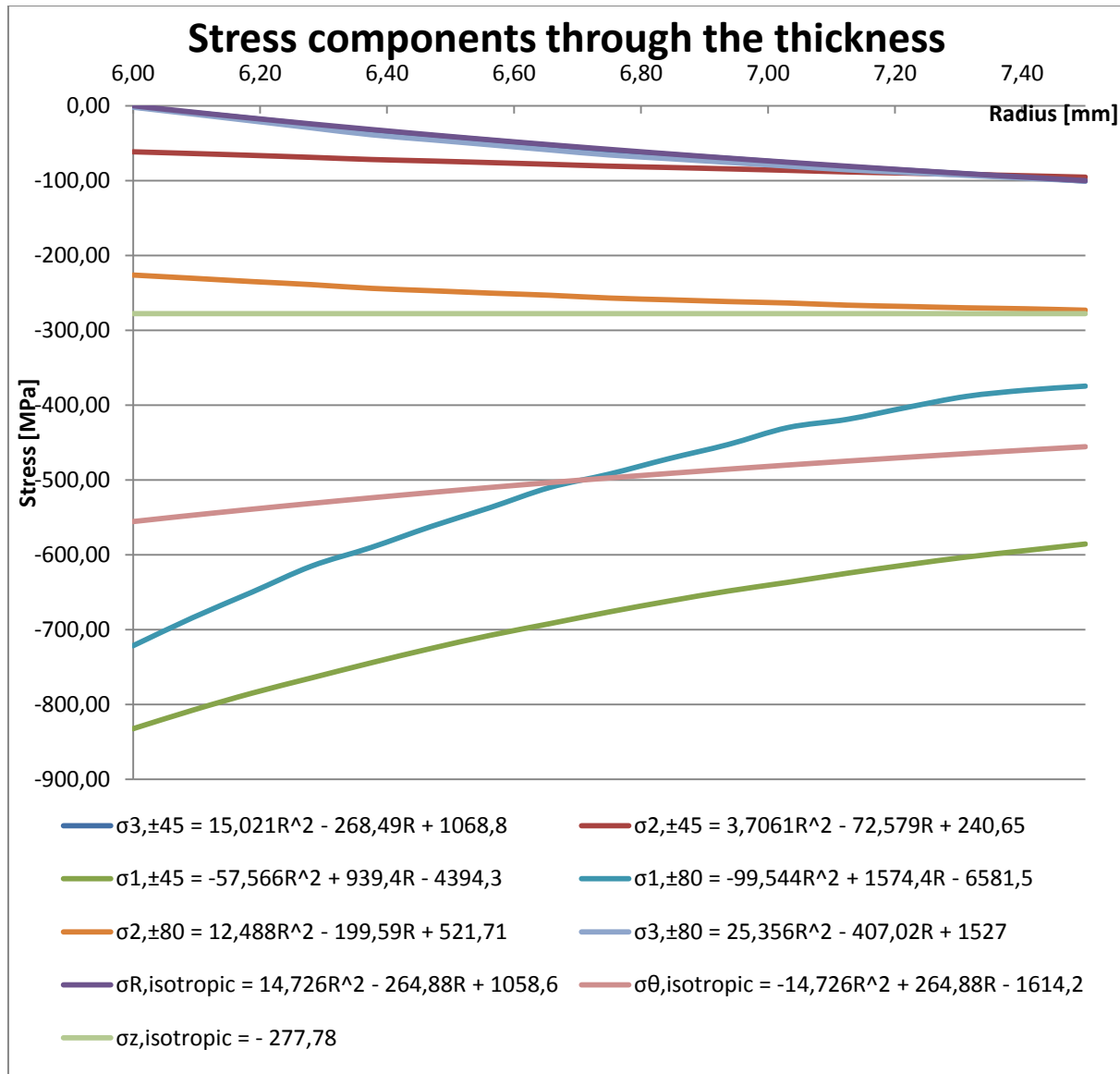
Figure 3-14: Stress components in the cross section area

These two approaches do not resemble each other since CFRP is an anisotropic material. Since the composite layup is rotated around the radial direction, only this axis will always be one axis in a plane of isotropy. The radial stresses are thus similar, and can be calculated with equation 3-4.

A calculation of the other components is mathematically extensive, and was not conducted in this thesis. It was still possible to verify the other stresses by obtaining an approach that considers the total load. In

Figure 3-14, polynomial approximation curves are obtained with their respective mathematic function. By integrating these functions with respect to the radius, the total force on the cross section area per millimeters in the circumference direction was obtained. Equation 3-7 yielded.

$$\sum_{n=1}^{3} \int_{6}^{7.5} \sigma_{n,FEM} \ (R) \ dR = \int_{6}^{7.5} \sigma_{\theta,iso} \ (R) \ dR + \int_{6}^{7.5} \sigma_{z,iso}(R) dR + \int_{6}^{7.5} \sigma_{R,iso}(R) dR \qquad \textbf{3-7}$$

The right side of equation 3-7 (the equations for an isotropic material) resulted in -1250 [N/mm] while the left side (the FEM results) resulted in -1234 [N/mm] for both models. A small deviation was expected since the FEM results were obtained from a Y-Y plot where data are extracted from a limited number of integration points, and that the functions were obtained from fitted curves.

To verify that the contact enforcements behaved as desired, any penetration of the contact surfaces were checked with the COPEN outputs. These data had all positive numbers, which proved that there were no penetrations. Visually, Abaqus showed some penetration at the interactions, but these could thus be regarded as a software visualization problem.

3.4.2   Failure prediction from Puck's failure criterion and eigenvalue problem
The critical pressures, P_{cr}, were obtained from three sections of each of the three models (the plug-end, the midsection and the lid-end) to verify consistency in the model and to detect any irregularities occurred due to the interactions. The different sections are shown in Appendix D. Table 3-4 lists the critical pressures obtained from the Max stress failure criterion, Puck's FF and IFF criterion. It also shows critical buckling loads. Max stress failure criterion was included for comparison, and it could be seen that this failure criterion is much more conservative than Puck's failure criterion.

Layup	Section	P_{cr} Max stress [MPa]	P_{cr} FF [MPa]	P_{cr} IFF [MPa]	P_{cr} Buckling (EV2) [MPa]	P_{cr} Buckling (EV4) [MPa]
$[\pm45°]_4$	Plug-end	-62,07	-133,30	-72,89		
$[\pm45°]_4$	Midsection	-66,93	-137,36	-80,45	-91,40	-97,63
$[\pm45°]_4$	Lid-end	-62,11	-132,62	-72,93		
$[\pm80°]_4$	Plug-end	-52,52	-179,21	-65,19		
$[\pm80°]_4$	Midsection	-54,91	-180,51	-76,69	-147,13	-152,38
$[\pm80°]_4$	Lid-end	-52,55	-179,21	-64,72		
$[\pm80°_2, \pm9°_2]$	Plug-end	-41,15	-113,38	-54.08		
$[\pm80°_2, \pm9°_2]$	Midsection	-112,11	-115,21	-392,15	-70,50	-75,21
$[\pm80°_2, \pm9°_2]$	Lid-end	-74,40	-113,51	-117,92		

Table 3-4: Numerical calculated critical pressures, high pressure FEM models

From Table 3-4 it could be seen that P_{cr} was lower at the ends than in the midsection for all models. This could be expected due to higher stress concentrations around the interactions. It could also be seen that the [±45°] and [±80°] models most likely would fail due to IFF, according to Puck's failure prediction, and

the [±80°$_2$, ±9°$_2$] model would most likely collapse due to buckling. All the buckling results showed good accordance with the discussion in Section 2.5.

It could be concluded that there was good consistency regarding the interactions due to the low variation of P_{cr} between the sections. Still, there was a small difference, which indicated that failure was likely to be expected at the ends. The low stress found at the plug-end of the [±80°$_2$, ±9°$_2$] model (highlighted in red) stood out as a very low value compared to the others. This value was found in the hoop layer at the very end of the tube. This prediction was very uncertain since it should have been the same situation for the corresponding area at the other end of the tube.

3.4.3 Failure location and stress components in critical areas

Both the [±45°] and the [±80°] model indicated that the failure was initiated at the inside wall of the tube. An example is shown in Figure 3-15.
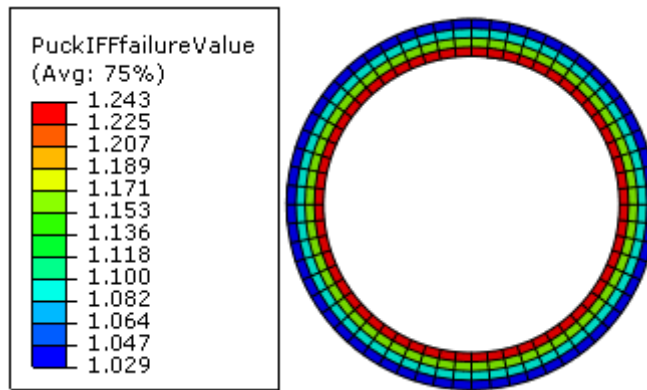
Figure 3-15: failure location predicted by Puck's failure criterion

From these critical elements, the stress components could be found. The stress components were obtained from the numerical results and scaled with the stress exposure factor to find the critical values. The critical stress components for the [±45°] model are shown in Table 3-5.

Section	σ_1	σ_2	σ_3	τ_{12}
MID	-669,6	-49,5	-1,1	94,8
PLUG	-572,9	-40,1	-0,7	94,0
LID	-572,7	-40,0	-0,7	94,0

Table 3-5: Critical stresses [MPa], inner ply, [±45°] layup

From Table 3-5, the τ_{12} stresses have clearly exceeded the shear stress strength (according to Table 3-3). This is as expected, since the dominating elastic modulus, and thus strength of a ±45° layup is shear. Figure 3-16 shows the $\sigma_2 - \tau_{12}$ envelope for the stresses in the plug-end and the lid-end and illustrates how Puck implements the influence of the transversal stresses to the material shear strength.

From Figure 3-16 it can also be seen that a small increase of stresses in τ_{12} allows for much more compressive stresses in σ_2, in accordance to the stress components in the midsection.
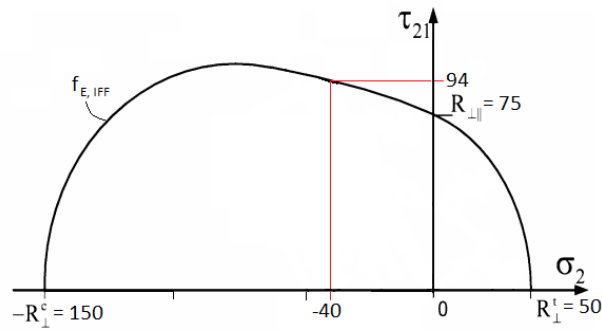
Figure 3-16: $\sigma_2 - \tau_{12}$ envelope of Puck's failure criterion

As the $\frac{\sigma_1}{-(R_\parallel^c)}$ ratio exceeded the weakening limit of 0.6 in the midsection, this should have some influence of the results. This was not implemented in the subscript that contained Puck's failure criterion, and could not be evaluated.

The critical stress components for the [±80°] model are listed in Table 3-6.

Section	σ_1	σ_2	σ_3	τ_{12}
MID	-553.2	-173.5	-1,5	23.8
PLUG	-354.5	-151.0	10.4	21.7
LID	-348.7	-153.0	12.7	22.1

Table 3-6: Critical stresses [MPa], inner ply, [±80°] layup

As seen from the results in Table 3-6, the dominating strength is the transverse compressive. In all sections, the stresses have exceeded the compressive transverse strength (according to Table 3-3). The numbers are still not consistent, since σ_2 in the midsection exceeds the strength more than the others without any major differences in the other stress components. This may be due to that the FEM model is modeled with layered elements, while the subscript containing Puck's failure criterion retrieves data from the whole element. This means that the subscript retrieves data from in the interval from the innermost ply till ply two and evaluates the most critical combination of these stresses. In the [±80°] model it was found that the critical σ_3 at the top of ply 2 was -25,6MPa. This justified the results. However, this error invalidated P_{cr} for the midsection. To find the actual P_{cr} for the midsection, the stress exposure factor was scaled up to where $\sigma_2 = 150Mpa$. While taking the influence of τ_{12} into account, P_{cr} was found to be 66.63MPa for the midsection. The $\sigma_2 - \sigma_3$ envelope with the final stress components can be seen in Figure 3-17.
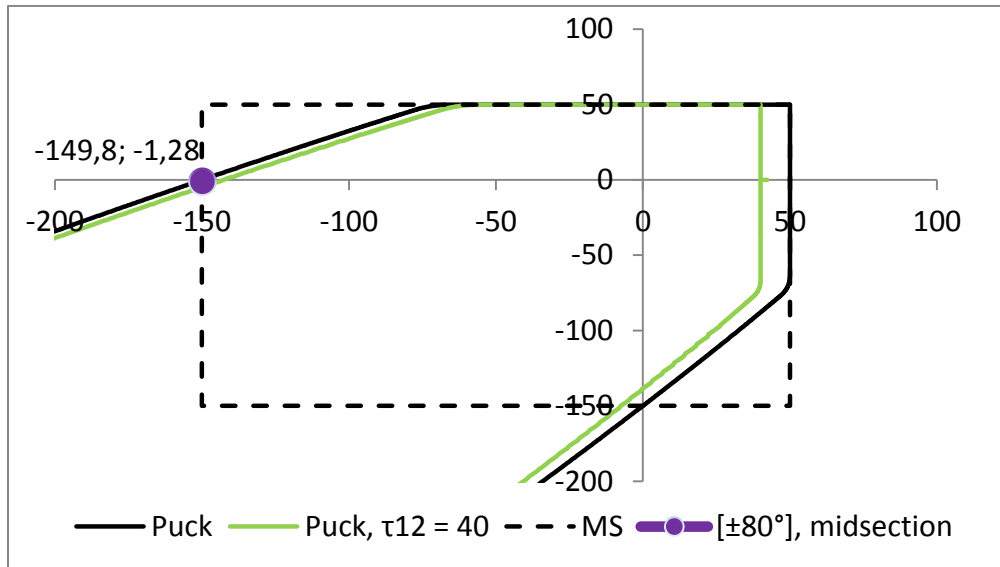
Figure 3-17: $\sigma_2 - \sigma_3$ envelope of Puck's failure criterion

While the stress concentration was wider spread at the ends of the [±45°] model, the stresses were more concentrated around the rounded parts of the plug and the lid for the [±80°] model. This is shown in Figure 3-18. This was due to the lack of fibers in the longitudinal direction of the [±80°] model, which resulted in reduced bending stiffness of the tube. This made it more likely that the [±80°] CFRP test samples would fail near the tube ends due to the plug and the lid, than in the middle.
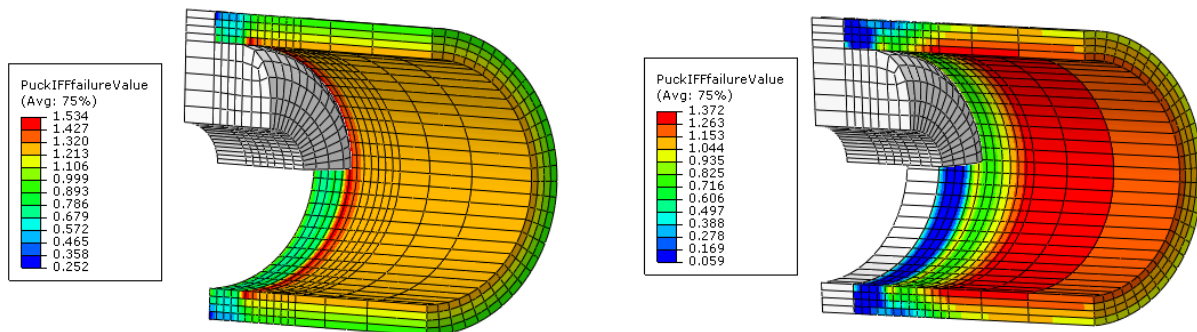
Figure 3-18: Stress concentrations

3.4.4 Strains

The axial and tangential strains of the [±45°] and [±80°, ±9°] models at $P_e = 100 MPa$ are listed in Table 3-7. The tangential strains are obtained from the inside wall of the tube.

	Axial direction		Tangential direction	
Model	**Strain (ε_z)**	P_e/ε_z	**Strain (ε_θ)**	P_e/ε_θ
[±45°]	8.95E-3	11170	-2.05E-2	4878
[±80°, ±9°]	-2.69E-3	37141	-8.02E-3	12463

Table 3-7: Strains from high pressure FEM models

31

By dividing P_e by the strains, a structural stiffness of the model was obtained. These results were to be used for comparison with the experimental results.

3.5 Numerical results for axial compression models

3.5.1 Model verification

The deformed model is shown in Figure 3-19. This deformed shape was satisfying since it resembled the shape of the deformed experimental test samples.
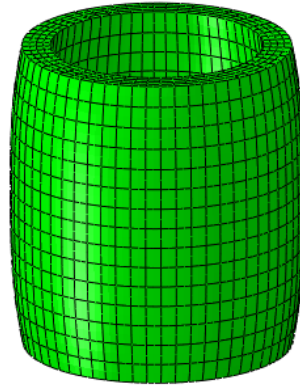
Figure 3-19: Deformed axial compression FEM model

To verify these results, the reaction forces at the constrained end were plotted from the *field output* and summarized with the Abaqus *operate on XY data* function. By dividing this sum on the cross section area, the stress was found to be equal to P_e for all models.

3.5.2 Results

Only P_{cr} and the failure modes are listed in Table 3-8.

Model	P_{cr} [MPa]	Failure mode
[±45°]	-143,88	Material, IFF
[±80°, ±9°]	-250,88	Buckling
[±80°]	-142,86	Material, IFF

Table 3-8: Numerical calculated critical pressures, axial compression FEM models

In contrast to the high pressure models, the location of the failure for the ±80° model is now on the outside surface of the tubes. For the ±45° model, the location is on the inside wall also this time. The [±80°, ±9°] model fails due to buckling.

The critical stress components for the models that fail due to material failure are listed in Table 3-9.

Model	σ_1	σ_2	σ_3	τ_{12}
[±45°]	-105.29	-6.72	-0.14	80.35
[±80°]	-113.06	-144,75	0	29.95

Table 3-9: Critical stresses [MPa], axial compression

From Table 3-9 it can be seen that σ_1 on the outside wall of the ±80° model is subjected to tensile stress. This is due to bending of the wall. The results are very similar to the high pressure testing results regarding the governing components; the ±80° model fails due to transverse stress, and the ±45° model fails due to shear stress.

3.5.3 Strains

The axial displacements and strains of the models at $P_e = 100 MPa$ are listed in Table 3-10. The structural stiffness in the axial direction is also included in Table 3-10.

Model	Displacement (δ_z) [mm]	Strain (ε_z)	P_e/ε_z
[±45°]	-0.117	-5.86E-3	17064
[±80°, ±9°]	-0.027	-1.35E-3	74074
[±80°]	-0.240	-1.20E-2	8333

Table 3-10: Strains from axial compression FEM models

While the structural stiffness of the ±45° is complex, some clear relations between the structural stiffness and the elastic moduli listed in Table 3-3 can be seen. Nearly half of the cross section area of the [±80°, ±9°] model contains close to longitudinal directed fibers. The other half is close to hoop wound fibers. This means that equation 3-8 should yield.

$$E_z = \frac{1}{A} \sum_{1}^{2} E_n A_n \qquad \text{3-8}$$

Inserting in equation 3-8 gives $E_z = 78252 MPa$. The ±80° stiffness can also be related; since the fibers is aligned almost in hoop direction, $P_e/\varepsilon_z \approx E_2$.

4 Experimental work

This chapter covers the experimental work carried out. This includes the process of manufacturing the test samples, microscopy analysis, experimental testing methods and an evaluation of the results.

Two methods were used for the experimental testing; high pressure testing and axial compression testing. The goal of both tests was to determine P_f, and to document the deformational strains in the samples. The results were then used to verify and substantiate the material strengths and elastic properties. All experimental work was conducted at room temperature.

Only the results from the [±80°] samples are presented here, since these samples were produced and tested in a previous work. One important note is that the production and evaluation procedure for these samples was the same as in this thesis.

4.1 Production of test samples

Samples with two different configurations were manufactured; they had different composite layups. All samples were wound with the filament winding machine at NTNU. The fibers were subjected to a tension of 14N during the feed time and impregnated in a resin-bath. The amount of excess resin was controlled with a blocking edge on the resin bath reel.

One meter long steel mandrels with a diameter of 12mm were used for the three different samples. They were covered with release agent and release wax to make the removal of the tubes as easy as possible.

Two tubes with a [±45°] layup were produced. This resulted in seven samples for high pressure testing and four samples for axial compression testing.

Four tubes with a [±80°, ±9°] layup were produced. This resulted in seven samples for high pressure testing and four samples for axial compression testing.

The outside diameters were manually measured during the winding, and all winding processes were ended when the outside diameter reached 15mm. The whole mandrel was uniformly covered at this point, and the results of the process looked satisfactory.

4.1.1 Curing and machining

The composite material was cured at two stages, according to the resin-data found in Appendix B. The first stage was with a heat lamp positioned above the rod while the rod was rotating. Given the time for the resin to become solid, approximately two hours, it is assumed the temperature was around 60°C. At the second stage the rod was cured in an oven at 140°C for two hours.

After the curing, excess epoxy had solidified on the outside surface and increased the outer diameter. The samples were thus sanded down to 15mm and cut into lengths at approximately 150mm and 20mm.

A series of photos from the production can be seen in Appendix E.

Pictures of the finished test samples for high pressure testing and axial compression testing are shown in Figure 4-1 and Figure 4-2, respectively.

Figure 4-1: Test samples for high pressure testing

Figure 4-2: Test samples for axial compression testing

4.2   Microscopy

Two samples were inspected with electron microscopy to check the production quality.

4.2.1   Samples with [±45°] layup

Figure 4-3 and Figure 4-4 show 50x zoomed microscopy images of the [±45°] samples.
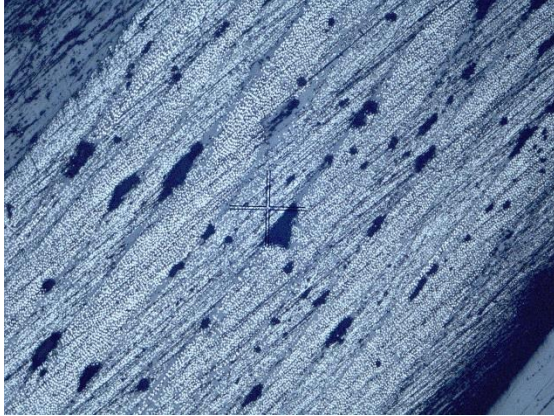
Figure 4-3: Microscopy of [±45°] samples, z-R plane cross section

Figure 4-4: Microscopy of [±45°] samples, θ-R plane cross section

4.2.2   Samples with [±80°, ±9°] layup

Figure 4-5 and Figure 4-6 show 50x zoomed microscopy images of the [±80°, ±9°] samples.
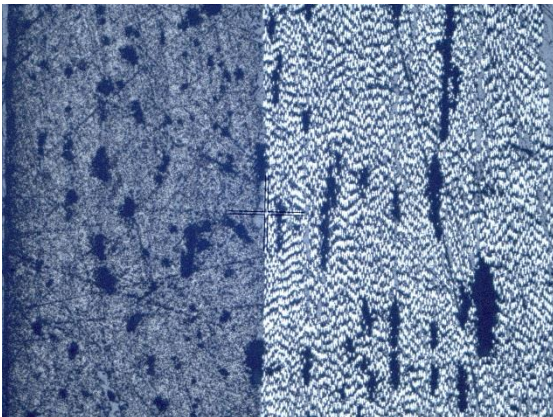
Figure 4-5: Microscopy of [±80°, ±9°] samples, z-R plane cross section
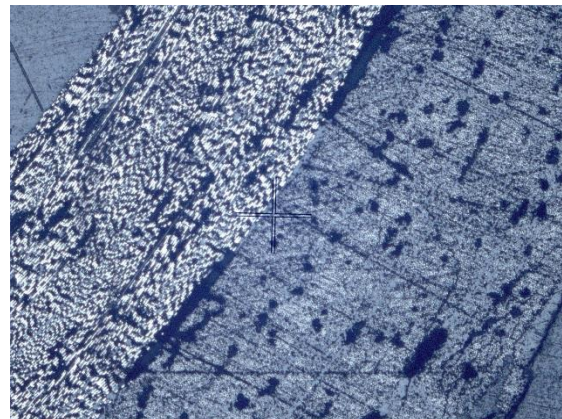
Figure 4-6: Microscopy of [±80°, ±9°] samples, θ-R plane cross section

4.2.3   Microscopy evaluation

Both samples showed a significant amount of voids. This was assumed to be because the rod was not treated with any vacuum or radial pressure to squeeze them out before curing started. The amount of voids was still at an acceptable level, so no attempt was made to reduce it.

The same could be seen from the microscopic analysis of the ±80° sample.

A significant amount of voids can be seen in the interface between the ±80^0 and ±9^0 layers on the [±80°, ±9°] test samples. This was of some concern, since this could have led to delamination.

4.3 High pressure testing

In short, the procedure for this testing method was to put the test samples into a closed and approximately rigid container and apply liquid into the system to increase the pressure. Time-pressure and time-strain data was logged digitally during the testing. At the end of the tests, the test samples failed due to the external pressure, and P_f could be found.

4.3.1 High pressure testing equipment

To test the samples with external pressure a high pressure pump was used. The pump was a Quizix C-5000-20K capable of pressures up to 20000psi. The pump has a cylinder volume of 5.2ml and was able to deliver fluids at a very accurate flow rate.

An autoclave for testing was made from solid steel. This device had to be designed regarding the following constraints:

- It had to be able to hold for an internal pressure up to 20000psi.
- The chamber had to be dimensioned to be able to fill the test samples' dimensions and surrounding liquid.
- To maintain atmospheric pressure inside the samples, one of the ends had to be in contact with the outside surroundings.

The body of the autoclave was dimensioned to be able to operate with test samples with outer diameters up to 17.5mm, whereas the lid was customized for the inner diameter of the samples. A notch was made in the autoclave body to fit an o-ring between the body and the lid. The test samples were glued with an epoxy to a tip on the lid with the same diameter as the inner diameter of the test samples, and then the lid was bolted to the body with 6 M8 bolts. This held the test samples fixed in the autoclave during testing. The test samples were also sealed with a plug at the top. The epoxy glue would work as sealing for the water, and the ends would then be closed due to the plugs and the external pressure. The full system setup is shown in Figure 4-7.

Due to the high pressures, an o-ring was used to seal the system from any leakage. The o-ring caused the system to expand although a completely rigid system would have been preferable.

The fluid used to pressurize the rod was distilled water. Before each test the system was completely filled and bled to make sure there was only water in the system. By using water, the volume needed to get high pressures was low, and 20000 psi could be obtained using only one stroke.
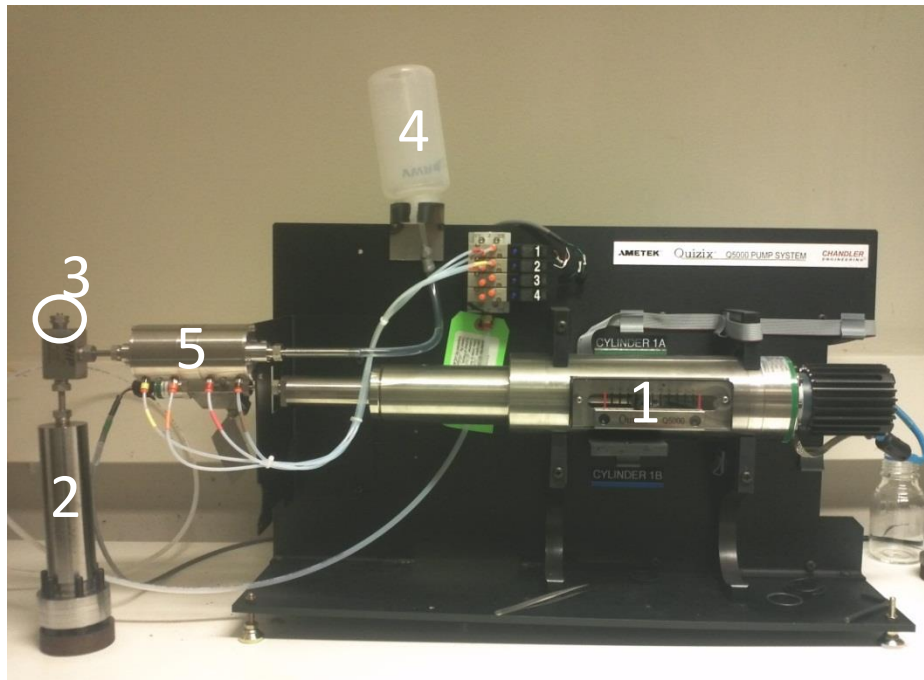
1	Pump
2	Autoclave
3	Bleed valve
4	Reservoir
5	Fill/deliver valve
6	Autoclave lid (lid tip circled)
7	End plug (rod)
8	Notch with o-ring
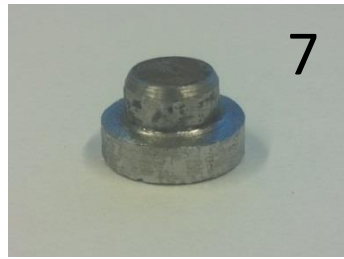
Figure 4-7: Pump setup

4.3.2 Optimization of test samples for high pressure testing

During pressure testing of tubes/cylinders, the end closures could be sources of stress concentrations. This could have caused failure in these regions, and affect the test results in an undesirable way. Since the samples were supposed to represent an infinite tube, the stresses should be uniformly obtained through the sample length. This could have been avoided by reinforcing the ends of the samples. But due to the production method of the test samples, this was not a feasible option. To best possible prevent this phenomenon the edges of the interacting plugs were rounded. This action, together with the assumption that the glue only had a sealing function (not fixing) allowed the samples to deform freely as much as possible.

Another challenge that could occur was leakage due to functional failure. If the samples were taking in water in the same rate as the pump provides it into the autoclave, there could have been a possibility that the samples never achieved structural failure. This was solved by adding a small layer of silicone sealant on the outside surfaces of the test samples.

Strain gauges were positioned on the inside wall of the test samples as illustrated in Figure 4-8. The strain data was processed with LabView Signal Express.

Figure 4-8: Strain gauge positions

4.3.3 Results from high pressure testing

Each test sample with data is listed in Table 4-1. All metrical measurements were done manually with a vernier caliper. The time-pressure curves can be found in Appendix F.

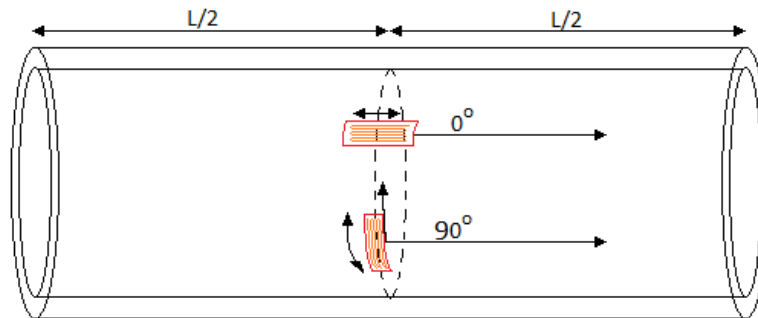| Sample #	Length [mm]	Outer diameter [mm]	Inner diameter [mm]	Layup	Flow rate [ml/min]	P_f [MPa]
1	150.00	15.15±0.05	12.00	[±45°]	0.5	65.88
2	150.25	15.10±0.05	12.00	[±45°]	0.5	62.55
3	149.85	15.05±0.05	12.00	[±45°]	1.0	71.27
4	150.70	15.00±0.05	12.00	[±45°]	0.5	63.53
5	149.15	15.10±0.05	12.00	[±45°]	1.0-2.0	72.90
6	150.00	15.10±0.05	12.00	[±45°]	1.0	71.32
7	149.90	15.05±0.05	12.00	[±45°]	0.5-7.5	72.70
8	150.75	15.60±0.10	12.00	[±80°,±9°]	1.0	61.08
9	149.75	15.50±0.05	12.00	[±80°,±9°]	1.0	71.35
10	150.40	15.45±0.15	12.00	[±80°,±9°]	1.0	72.68
11	149.80	15.55±0.05	12.00	[±80°,±9°]	1.0	70.74
12	150.00	15.55±0.00	12.00	[±80°,±9°]	1.0	69.50
13	149.70	15.35±0.05	12.00	[±80°,±9°]	1.0	75.70
14	152.20	15.35±0.05	12.00	[±80°,±9°]	1.0	70.22

Table 4-1: Test sample data and results from high pressure testing

The diameters listed in Table 4-1 were measured at the midpoint of the samples. It was noticed that the diameter was slightly larger at the ends of some of the samples. This could have been caused due to the cutting and the adjustment of the ends to make the sample-ends perpendicular to the walls of the tubes. In that case, the inner diameter should also have been affected. Since the inner diameter was measured to be 12,00mm at all ends, the cause is more likely to be the smoothening process. This process was done manually before the samples were cut. Due to the transition length during manufacturing, the ends

of the uncut batch had a slightly larger diameter at the ends. It is not easy to determine whether this was just excess epoxy or additional fiber reinforcement. These dimensional effects may have influenced the results.

Another challenge that was encountered during the high pressure testing was leakage in the interaction between the test samples and the lid of the autoclave. Due to this, some of the samples were tested more than once. It also led to the need of increasing the flowrate during the test to achieve structural failure. It was difficult to measure how this affected the results.

All [±45°] samples had a visually clear failure parallel to the fiber direction. The location of failure was found at various locations along the length, but tended to be near the ends. This was in good accordance with the numerical analysis. Some failed [±45°] samples are shown in Figure 4-9.

Figure 4-9: Failed [±45°] samples after high pressure testing

Figure 4-10: Failed [±80°, ±9°] samples after high pressure testing

The [±80°, ±9°] failed more catastrophic, as can be seen in Figure 4-10. The failure was both parallel and transverse to the fibers, and a distinct hole through the thickness could be seen on some samples. This indicated that the samples failed due to buckling.

For the [±45°] samples, different flowrates was used. From Table 4-1 it can be seen that the samples with flowrate 0.5ml/min failed prior to the ones with a higher flowrate. This may indicate that the samples show viscoelastic behavior. The work of Koyanagi J. (2011) [25] shows that the strength of composites increases with the strain rate until a certain limit, which is shown in Figure 4-11. This subject was not included in this thesis, but it may explain the correlation between strength and stress/strain rate. Due the uncertainty on this matter, the average failure stress for each layup configuration was used for further discussion.
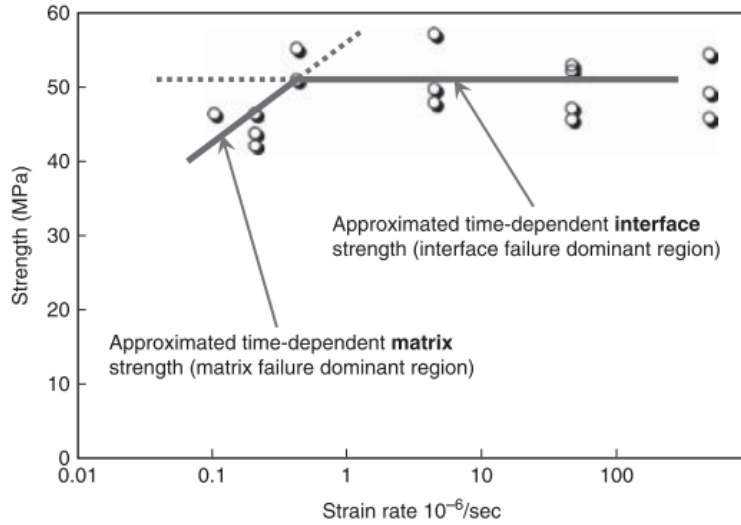
Figure 4-11: Viscoelastic influence on structural strength

Two samples of the high pressure testing had successful strain results. The stress-strain curve for one of the [±45°] samples is shown in Figure 4-12. This data are obtained from an unsuccessful test where the sample did not fail due to leakage. However, it can be seen that the axial strain was positive, in good accordance with the numerical model. Due to the nonlinearity of the curve, an approximation of the structural stiffness in the axial direction was not conducted.
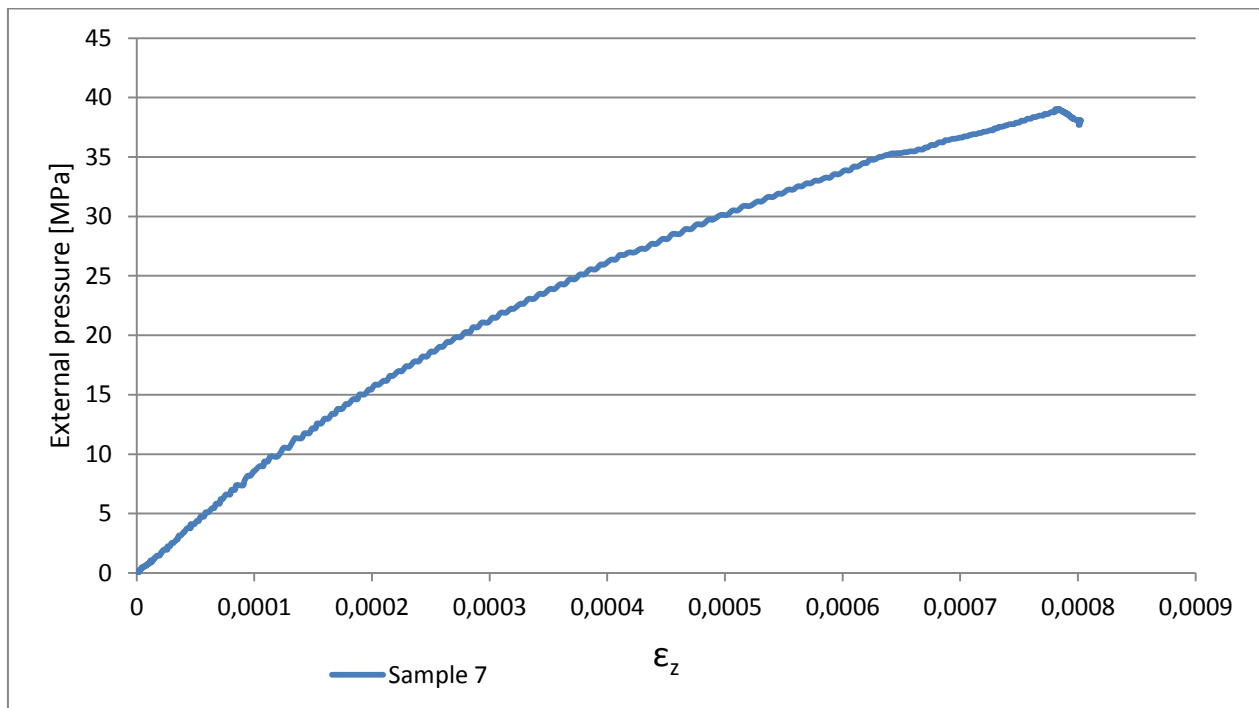
Figure 4-12: Stress-strain curve, high pressure testing, [±45°]

One of the [±80°, ±9°] samples had more successful results from the strain logging which can be seen in Figure 4-13. These curves showed much more linearity, and an approximation of the structural stiffness in the tangential and axial direction could be obtained. These were found to be 28714MPa and 57070MPa, in the tangential and axial direction, respectively.
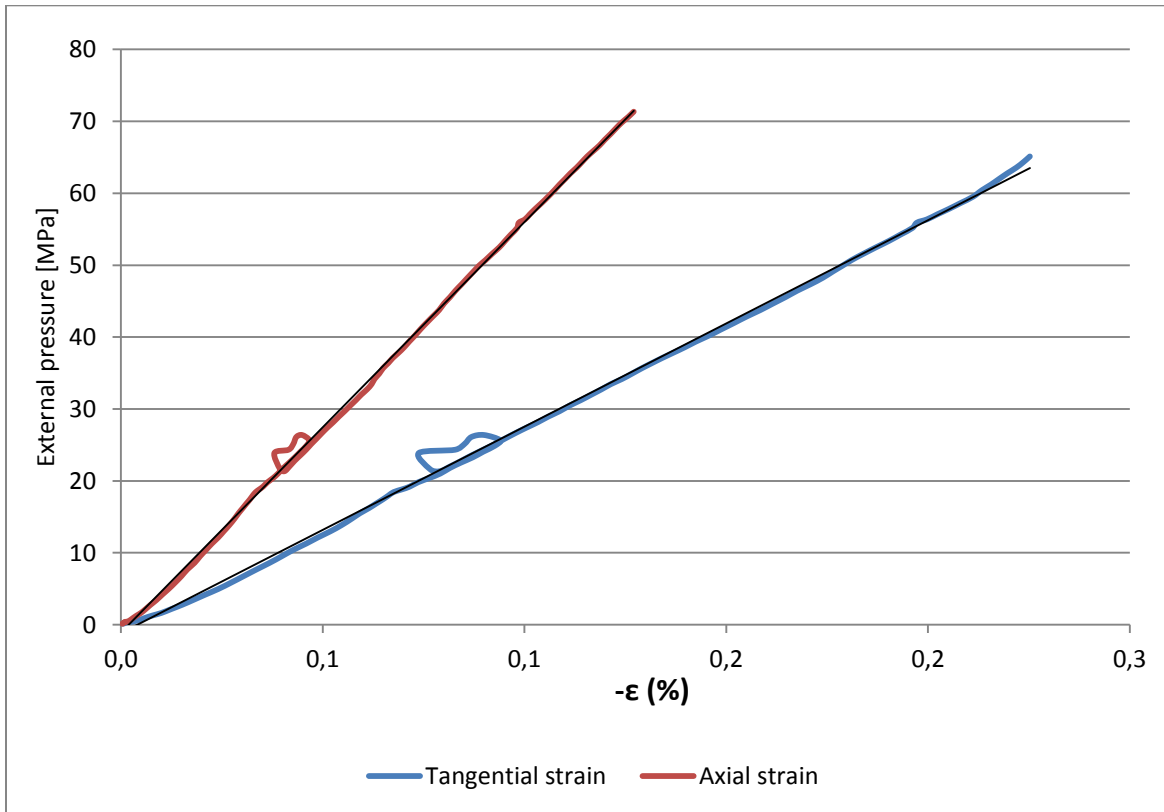
Figure 4-13: Stress-strain curve, high pressure testing, sample 9, [±80°,±9°]

4.4   Axial compression testing

The axial compression tests were done with the goal of measuring P_f for the samples in a pure axial compression state. The strains of the samples were also to be documented, for comparison with the numerical analysis.

4.4.1   Axial compression testing equipment

The axial compression testing was done using the Instron model 1342 hydraulic test rig at NTNU. The end faces of the samples were made parallel and perpendicular to the tube wall in a lathe. This was essential to ensure an evenly distributed load throughout the cross section area. The samples was then put between two thick plates of steel and compressed at a rate of 0,5mm/min. The data was processed with LabView Signal Express. The load output was in kN, so the results were transformed into stress by dividing the load with the actual test sample cross sectional area. The test setup is shown in Figure 4-14.

Figure 4-14: Axial compression test setup

4.4.2   Results from axial compression testing

The course of events was visually the same for all test samples; the friction between the samples and the plates kept the original cross section area from deforming, while the wall of the test samples was bulging outwards, resulting in deformation into a barrel-shape. It could also be seen that some crushing was initiated at the top end (at the pushing end) on the [±80°, ±9°] samples before it reached maximum load capacity.

The results from the axial compression tests are listed in Table 4-2. All metrical measurements were done manually with a vernier caliper.

Sample #	Length [mm]	Outer diameter [mm]	Cross section area [mm^2]	Layup	Load rate [mm/min]	P_f [MPa]	$R_{0,5\%}$ [MPa]
1	19.45	15.15±0.05	67.17	[±45°]	0.5	-159.39	-133
2	20.25	15.15±0.05	67.17	[±45°]	0.5	-164.00	-125
3	20.05	15.15±0.05	67.17	[±45°]	0.5	-158.49	-122
4	20.65	15.15±0.05	67.17	[±45°]	0.5	-161.01	-130
5	21.00	15.55±0.10	76.81	[±80°,±9°]	0.5	-174.13	
6	19.00	15.55±0.10	76.81	[±80°,±9°]	0.5	-222.33	
7	19.60	15.55±0.10	76.81	[±80°,±9°]	0.5	-217.73	
8	19.70	15.55±0.10	76.81	[±80°,±9°]	0.5	-261.61	

Table 4-2: Test sample data and results from axial compression testing

The results from the [±45°] samples were very satisfactory. The failure stresses varied little, and showed great consistency. Average P_f for the [±45°] samples was -160.72MPa. The stress-strain curves for these samples are shown in Figure 4-15.
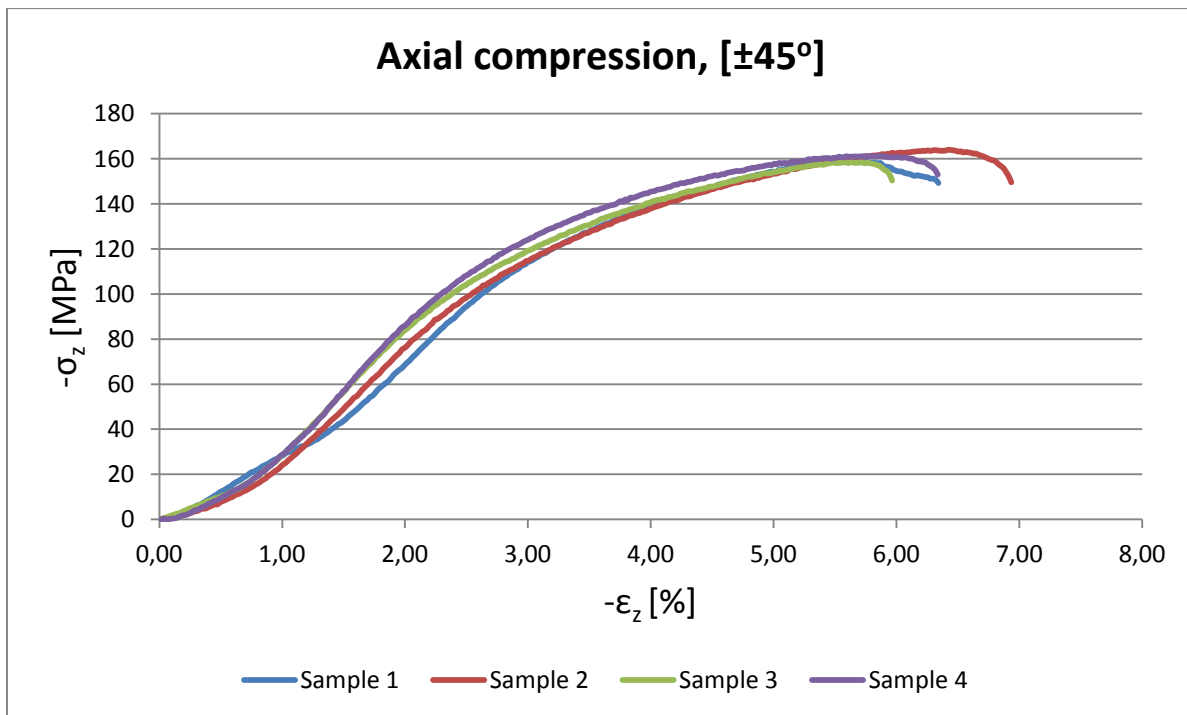
Figure 4-15: Stress strain curve for the [±45°] samples, axial compression testing

As noted for the high pressure testing, the material had viscoelastic properties. This affected probably also the results from the axial compression tests due to the low compression (strain) rate. The stress-strain curves in Figure 4-15 were nonlinear and failed after plastic deformation. This indicated that the material also is transversally ductile. The compressive shear response of ±45° composite laminates tends to be nonlinear, which can be seen in Figure 4-16 [26]. Figure 4-17 shows two of the failed [±45°] samples.
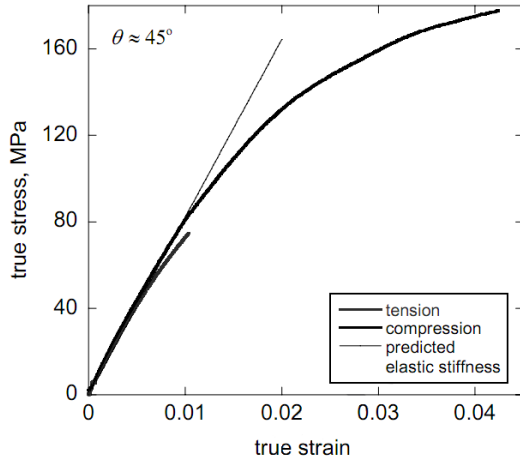
Figure 4-16: Shear response
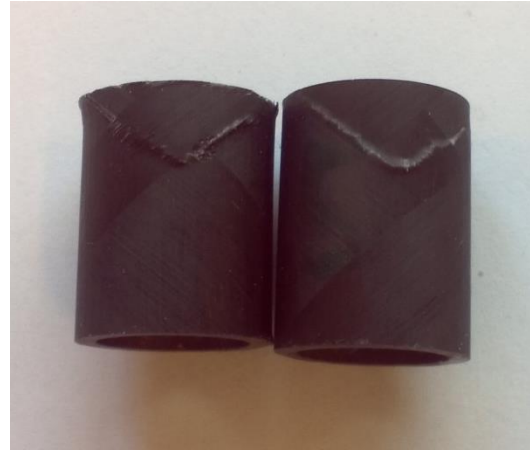
Figure 4-17: Failed [±45°] samples after axial compression testing

Due to the nonlinearity of the stress-strain curves for the [±45°] samples, proof stress, $R_{0.5\%}$, was determined by the offset method. The chosen offset was a strain of 0.5%, which was found satisfactory. The elastic slope was determined from the linear parts of the stress-strain curves. An example of this is shown in Figure 4-18. $R_{0.5\%}$ for all the [±45°] samples are listed in Table 4-2, and the average elastic slopes (approximated structural stiffness in the axial direction) was found to be 5561MPa.
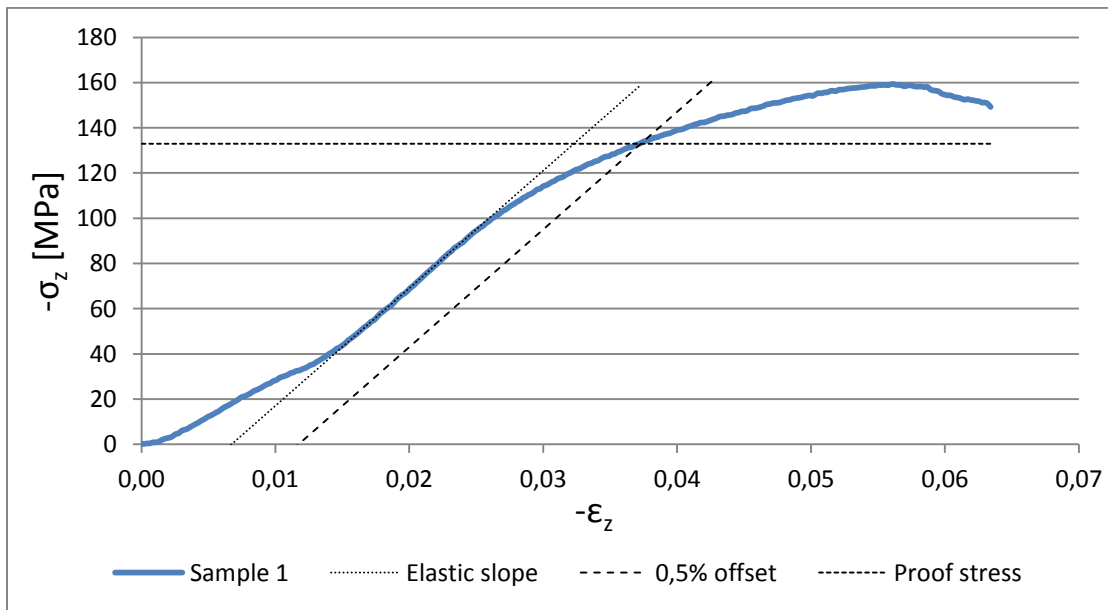
Figure 4-18: Determination of proof stress

The stress-strain curves of the [±80°, ±9°] samples are shown in Figure 4-19. P_f for the [±80°, ±9°] samples had large variation. Average P_f for these results was 218.95MPa.
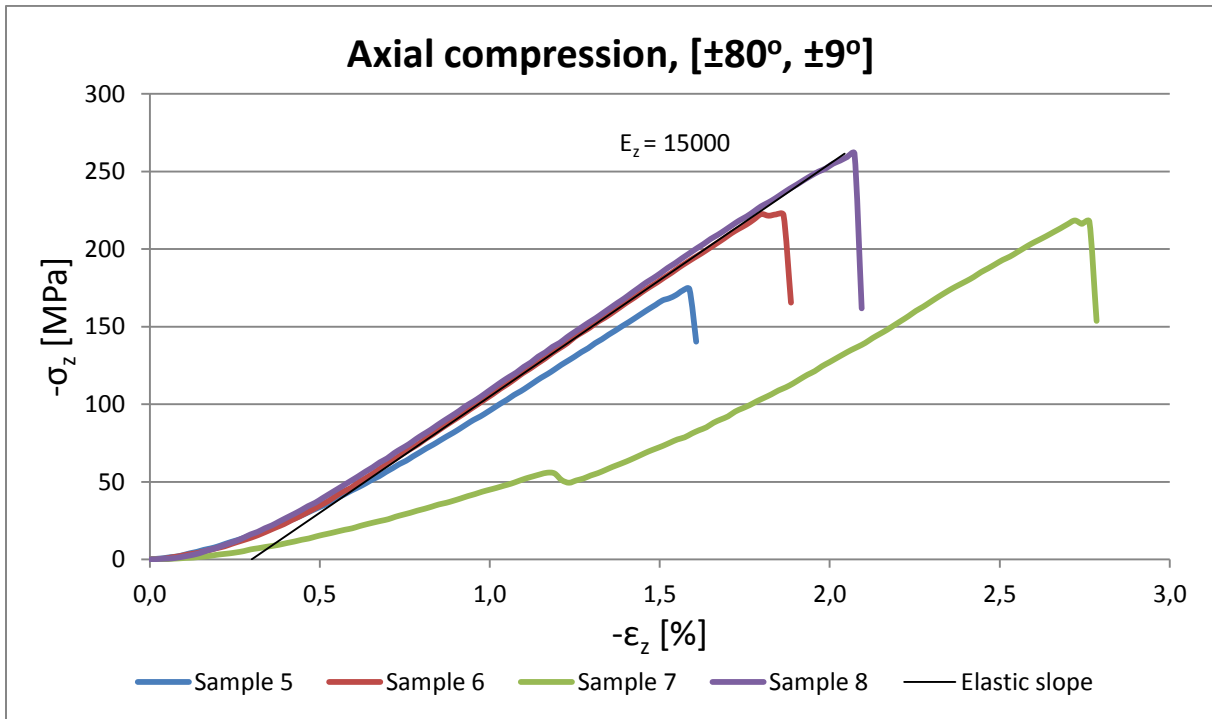
Figure 4-19: Stress strain curve for the [±80°, ±9°] samples, axial compression testing

These results showed much more linearity, which probably were due to the ±9° fibers. The load was directed close to normal to the fibers, which are brittle and very stiff. Sample 7 stood out with its low and varying stiffness. This was possible due to non-parallel end surfaces, which led to longer time for the load to engage the whole cross section area. The approximated structural stiffness in the axial direction was 15000MPa.

Some local crushing was observed at the ends of the [±80°, ±9°] samples. This was probably due to that the hoop layers acted as a radial support for the longitudinal layers, and when the hoop layer failed the longitudinal layers delaminated at the ends due to the increased local stress in these areas. This can be seen in Figure 4-20, which shows the samples after testing.
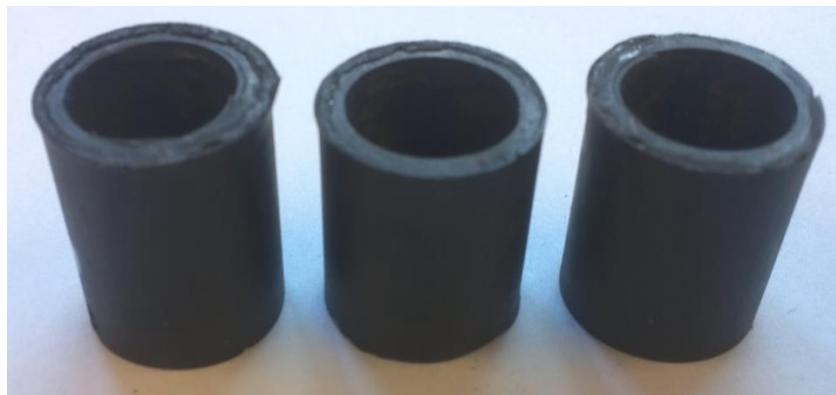
Figure 4-20: Failed [±80°, ±9°] samples after axial compression testing

46

Without any strain gauges, the strain measurements were not completely reliable. Both due to that the ends of the samples were not perfectly parallel, and due to bending of the steel plates. This made the approximated structural stiffness in the axial direction for all axial compressed samples significantly lower than expected.

As seen from Figure 4-15 and Figure 4-19, the stress did not engage the whole cross section area of the samples in the beginning, which led to a nonlinear first part of the stress-strain curves.

4.5 Results from previous work

The high pressure testing results for the [±80°] samples are listed in TABLEXX.

| Sample #	Length [mm]	Outer diameter [mm]	Inner diameter [mm]	Layup	Flow rate [ml/min]	P_f [MPa]
1	150	15.00	12.00	[±80°]	0.5	-73.65
2	150	15.00	12.00	[±80°]	0.5	-77.38
3	150	15.00	12.00	[±80°]	0.5	-69.39
4	150	15.00	12.00	[±80°]	0.5	-74.65
5	150	15.00	12.00	[±80°]	0.5	-75.20
Average P_f [MPa]:						-74.05

Table 4-3: Test sample data and results from high pressure testing for the [±80°] samples

Since the dimensions of these samples were not accurately measured, the theoretically dimensions are shown. The high pressure testing time-stress curves of the [±80°] samples are shown in Appendix F.

These samples failed at both the ends and at the middle of the tube.

No graphs are available from the axial compression tests from the previous work. The data were read live from the digital display on the machine. The tests were done with a compression rate of 0.3mm/min and they were aborted when the load level read from the display stabilized. At this point the material's load capacity was exceeded. The obtained data from this test is shown in Table 4-4.

Sample no.	Length [mm]	Maximum load [N]	Cross section area [mm²]	P_f [MPa]
1	20	-9000	63.61	-142.5
2	20	-9500	63.61	-150.4
3	20	-9000	63.61	-142.5
	Average P_f [MPa]:			-145.13

Table 4-4: Test sample data and results from axial compression testing for the [±80°] samples

5 Result evaluation and discussion

5.1 Comparison of P_{cr} and P_f

Due to the varying failure locations of the experimental high pressure test samples, each numerical model were evaluated to find which section of the FEM model the results were to be obtained from;

- P_{cr} for the [±45°] model was taken from the end sections of the FEM model since the experimental failure locations tended to be located in these areas. The less conservative P_{cr} of these was used (-72.93MPa).
- P_{cr} for the [±80°] model was taken from the midsection of the FEM model since the experimental failure locations were located at various points all over the sample length.

The numerical and the experimental results are summarized, compared and listed in Table 5-1 and Table 5-2.

Layup configuration	P_{cr} [MPa]	Average P_f [MPa]	Difference* [%]
[±45°]	-72.93	-68,59	6.0
[±80°,±9°]	-70,50	-70,18	0.45
[±80°]	-66.63	-74.05	-11.1
* $(P_{cr} - P_f)/P_{cr}$			

Table 5-1: Numerical and experimental high pressure test results with differences

Layup configuration	P_{cr} [MPa]	Average P_f [MPa]	Difference* [%]
[±45°]	-143,88	-160.72	-11.7
[±80°,±9°]	-250,88	-218.95	12.7
[±80°]	-142,86	-145.13	-1.5
* $(P_{cr} - P_f)/P_{cr}$			

Table 5-2: Numerical and experimental axial compression test results with differences

For both the axial tests and the high pressure tests, the [±80°, ±9°] samples failed prior to P_{cr}. The percentage error for the axial compression tests were higher than for the high pressure testing, which is probably due to the experimental testing method, which is discussed in section 4.4.2. It was expected that the numerical calculated P_{cr} was higher than P_f since the numerical buckling calculations were based on an ideal geometry without imperfections. In addition to non-ideal testing procedures, the microscopy analysis and the test sample measuring proved errors in the geometry and the material. This explained the lower P_f. Still, the difference was relative low, and in could be concluded that the structure was well modeled and the assumed elastic moduli were reasonable.

The deviation in the high pressure results for the [±80°] samples was higher than expected. Since P_{cr} was lower than P_f, it could indicate that the actual transversal strength of the material was higher than first assumed. The axial compression tests failed however very close to P_{cr} and could be stated as a very satisfying result. Also these differences were negative, but with a much lower percentage. The

inaccurate logging of data during the axial compression tests of the [±80°] decreased the reliability of these results, but they were evaluated to be accurate enough for this investigation.

The [±45°] samples had satisfying results for the high pressure testing. The 6% difference may be explained by saying that the assumed shear strength of the material was a little too high. On the contrary, the axial testing showed much lower P_{cr} than P_f. This was probably because the numerical model did not account for a nonlinear shear response and ductility. The FEM model was calculated as linear-elastic, hence too stiff.

5.2 Statistical significance

For designing purposes, an average P_f might be misleading with high statistic uncertainty. The characteristic value P_{char} is often used in experimental works, which gives a 95% probability that the test sample will hold for greater loads. This value is better fitted as a design parameter. The characteristic strength value is calculated from equation 5-1.

$$x_c = \bar{x} - k_m \hat{\sigma}$$
5-1

In equation 5-1, $\bar{x}$ is the average load, $\hat{\sigma}$ the standard deviation, and k_m a factor for calculating characteristic value when you have a given amount of samples. K_m was found to be 4.3 for 6 samples. The closer the characteristic value is to the obtained P_f, the better. The characteristic values for the high pressure testing are listed in Table 5-3.

Test samples	P_{cr} [MPa]	Average P_f [MPa]	P_{char} [MPa]
[±45°]	-72.93	-68,59	-50.06
[±80°, ±9°]	-70.50	-70,18	-51.96
[±80°]	-66.63	-74.05	-61.13

Table 5-3: Characteristic values compared to P_{cr} and P_f

High pressures set a higher demand to the quality of the material. Small imperfections in the material or weaknesses in the interfaces due to human errors could be more critical when testing at such high pressures. The microscopy revealed that the material did not have a critical amount of voids. For the [±80°, ±9°] samples, voids were found to be in the interference between the two laminates, which could lead to delamination. This may explain the low P_{char} for these samples. The deviations for the axial compression tests were even higher for these samples, which only strengthens this suspicion. Other possible imperfections in the material could be microscopic cracks. This has not been analyzed, and is therefore impossible to evaluate at this stage.

Another important factor for these results relied on viscoelastic effects. This was an issue for the [±45°] sample's high pressure results, as discussed in section 4.3.3. This effect clearly made an impact on these results due to the different flowrates, which led to high deviation. Still, using Puck's failure criterion the results from the [±45°] sample tests were in good consistency with the failure theory. Lower deviation in the results was found for the [±80°] sample tests where the same flowrate was maintained throughout the testing.

The high characteristic value obtained for the high pressure tests proved however a relatively good statistical significance due to the low number of test samples.

For the axial compression tests, the number of samples was too low for the characteristic value to be regarded as a valid statistic design parameter. The [±80°, ±9°] samples proved to be superior to the others regarding strength. However, the high variation of P_f and the low number of test samples would lowered the characteristic value for the [±80°, ±9°] samples which gave these results no statistical significance.

5.3 Strains and structural stiffness

A summary of the calculated and approximated structural stiffnesses are listed in Table 5-4.

Model	Numerical calculated P_e/ε				Experimental approximated P_e/ε			
	High pressure test		Axial compression test		High pressure test		Axial compression test	
	z-direction	Θ-direction	z-direction	Θ-direction	z-direction	Θ-direction	z-direction	Θ-direction
[±45°]	11170	4878	17064	NA	NA	NA	5561	NA
[±80°, ±9°]	37141	12463	74074	NA	57070	28714	15000	NA

Table 5-4: Calculated and approximated structural stiffnesses

The strain measurements and the approximated structural stiffnesses were not as successful as the loads. While the experimental axial compression results showed much less stiffness than calculated, the experimental high pressure results showed higher stiffness than calculated.

The axial compression tests were conducted without strain gauges. The Instron machine logged its own piston displacement. By evaluating these results with other users of this machine, it was found that the machine logged wrong displacement data, either due to software or hardware error. Due to the measuring method, not only the sample displacement was logged but the whole system. The measuring method was thus dependent of the rigidity of the whole system. It was also found that the machine provides correct logging of the loads. This means that without strain gauges, these data were invalid.

The high pressure strain results showed much more stiffness in the experimental test samples than in the numerical model. Since the calculated and experimental buckling results had very good consistency, the assumed elasticity properties of the numerical model could not be very off. One explanation of this is that the strain gauges were not perfectly positioned in the axial and hoop directions. Since the [±45°] samples expanded in the axial direction and contracted in the hoop direction, a small deviation from their representative axis has a great impact on the results. An accurate measurement of the actual angles of the strain gauges was found to be difficult, so this could not be proved.

5.4 Evaluation of optimal layup configuration

As seen from the numerical results in Table 3-4, the precence of longitudinal-alligned fibers drastically improved P_{cr} regarding material failure, at the expence of buckling strength. The pressure capacity

treshold of 100MPa seemed to be somewhere between an angle of ±45° and ±80° regarding bucling, but the structure would fail due to material failure with these layups.

This discussion lead to the obvious that a simple [±θ] layup would not hold for this application. To maintain the stability and to overcome the high hoop stresses on the inside of the tube, a portion of hoop-alligned fibers seemed to be an obvious choice. But since the [±80°] failed due to transverse stresses, a portion of the thickness must also contain some longitudinal fibers . As discussed in section 2.5, the critical buckling pressure increases with the hoop/longitudinal ratio. As the [±80°, ±9°] samples failed due to buckling, this ratio had to be larger than one. This ratio was not investigated any further.

The material has a great potential for the use in oil-well environment, but for the given geometry, its pressure capacity was below the design criterion of 100MPa. The submerged weigth criterion stated that the inner diameter had to be 9.81mm for the tube to behave as desired in an oil well. This means that an additional cross section area of 40.4mm^2 was desired. If this is added on the outside wall of the tube, the outer diameter will be 16.63mm.

If this additional CFRP is a layup in the longitudinal direction, the bending stiffness criterion might be satisfied. By combining equations 2-3 and 2-4, equation 5-2 yields for finding the axial stress due to bending.

$$\sigma_{max} = \frac{M_R}{I_z} \cdot r_o = \frac{\sum_1^2 E_n I_n}{I_{tot} \cdot R} \cdot r_o \qquad \qquad \text{5-2}$$

With pure hoop in the interval $6 \leq r \leq 7.5$ and longitudinal fibers in the interval $7.5 < r \leq 16.63/2$, equation 5-2 gives an max axial stress of 274.1MPa, which is mutch less than the longitudinal compressive strength of the material. This will thus satify the design criteria of both bending stiffness and submerged weight. With this additional material, the pressure capacity of the tube will probably exceed 100MPa.

5.5   Future work

There are several things that would need a deeper investigation on this subject. Time dependent properties are mentioned as factors that could affect the results. This was not studied any further, but since the tube is subjected to constant bending during storage, creep is an important study. This also leads to the need for a proper bending test.

Studies of a wider range of layups should be conducted to obtain better statistics on the failure modes.

The temperature inside an oil well can reach hundreds of degrees Celsius while it may fall down to zero degrees in deep ocean water. This factor is therefore strongly dependent on the application, and should be taken into account when dimensioning the tube. The degree of influence that temperature affects the pressure capacity of the material is an important study which should be conducted.

6   Conclusions

The main focus of this task was to study the behavior of relevant thick-walled fiber composite tubes subjected to external pressure employing both numerical and experimental methods. Three principal composite layups were analyzed, both numerically and experimentally by high pressure testing and axial compression tests. Test samples were produced and evaluated for these tasks, and compared with results from representative finite element models.

Puck's failure criterion was implemented in the numerical calculations. This failure criterion proved to obtain very coherent results, and it described the material strength in compression very well. By an investigation of the stress components, it was found that Puck's failure criterion predicted that the $[\pm 80^{o}]$ samples failed due to transversal tresses and the $[\pm 45^{o}]$ samples failed due to shear stresses. The $[\pm 80^{o}, \pm 9^{o}]$ samples failed due to buckling.

All samples for both test methods failed very close to the predicted failure loads with relatively low percentage difference. The differences were found to be between -11.1% and 12.7%. After an evaluation these results, it could be concluded that the strength and elasticity parameters of the material was reasonably assumed and that the experimental testing procedures was well fitted for the study of the behavior of composites subjected to compression.

Strain measurements were also conducted in this thesis. These results were unsuccessful, and they proved that strain gauges are essential for this kind of measurements, but they require accurate positioning.

Based on these results, a discussion of an optimized structure was conducted. It was found that the buckling strength increased with an increased portion of fibers in the hoop direction of the tube while it at the same time decreased the material strength due to the axial stress. The geometry analyzed in this thesis had much higher buoyancy than desired for the application. It could thus be concluded that filament wound carbon fiber reinforced polymer tubes are well suited for the use in oil-well environment and shows great potential regarding pressure capacity.

7 Bibliography

1.   Agency, I.E., *World Energy Outlook.* 2008: p. 197.
2.   Yousif, H.R.a.O., *Buckling of Thin Laminated Orthotropic Composite Rings/Long Cylinders Under External Pressure*. 2001.
3.   S. Gohari, A.G., M. Mostakhdemin, F. Mozafari, and A. Momenzadeh , March 2012, *Failure Strength of Thin-walled Cylindrical GFRP Composite Shell against Static Internal and External Pressure for various Volumetric Fiber Fraction.* International Journal of Applied Physics and Mathematics, 2012. **2**(2).
4.   White, F.M., *Fluid Mechanics*. 2003: McGraw Hill.
5.   MatBase. *Material properties database*. 2009; Available from: http://www.matbase.com/material/other/fuel/crude-oil-north-sea/properties.
6.   Hoa, S.V., *Principles of the Manufacturing of Composite Materials*. 2009, DEStech Publications p. 13-14.
7.   Ahmad, J., *Machining of Polymer Composites*. 2009: Springer Science+Business Media, LLC.
8.   Hoa, S.V., *Principles of the Manufacturing of Composite Materials*. 2009, DEStech Publications. p. 207-208.
9.   Knops, M., *Analysis of failure in fiber polymer laminates: The theory of Alfred Puck*. 2008. p. 117.
10.   Dowling, N.E., *Mechanical behavior of materials*. 2007: Pearson Prentice Hall.
11.   Knops, M., *Analysis of failure in fiber polymer laminates: The theory of Alfred Puck*. 2008. p. 39.
12.   Knops, M., *Analysis of failure in fiber polymer laminates: The theory of Alfred Puck*. 2008. p. 45.
13.   Knops, M., *Analysis of failure in fiber polymer laminates: The theory of Alfred Puck*. 2008. p. 25.
14.   Knops, M., *Analysis of failure in fiber polymer laminates: The theory of Alfred Puck*. 2008. p. 77.
15.   Knops, M., *Analysis of failure in fiber polymer laminates: The theory of Alfred Puck*. 2008. p. 100.
16.   Irgens, F., *Fasthetslære*. 1999, Tapir. p. 386.
17.   Highsmith, E.G.a.A.L., *Compression response of composite structures*. 1994. p. 10-22.
18.   *Analysis of composite structures, section 1.1.4; Thick composite cylinder subjected to internal pressure*, in *Abaqus Benchmarks manual*.
19.   *Solid (continuum) elements, section 27.1.1* in *Abaqus Analysis User's Manual*.
20.   Matweb. *Material properties database*. Available from: http://www.matweb.com/search/DataSheet.aspx?MatGUID=d1bdbccde4da4da4a9dbb8918d783b29&ckck=1.
21.   Knops, M., *Analysis of failure in fiber polymer laminates: The theory of Alfred Puck*. 2008. p. 21.
22.   *Abaqus 6.11 documentation, section 12.13.4*.
23.   *Creating solid composite layups, section 12.13.4* in *Abaqus/CAE User's Manual*.
24.   Irgens, F., *Fasthetslære*. 1999, Tapir. p. 60.
25.   J., K., *Micromechanical modeling of time-dependent failure in off-axis polymer matrix composites*. 2011, Institute of Space and Astronautical Science, Japan. p. 11.
26.   Tagarielli, V.L., Minisgallo, G., McMillan, A.J., Petrinic, N., *The Response of a Multi Directional Composite Laminate to Through-Thickness Loading*, in *Composites Science and Technology*. 2010.

TORAYCA®
T700S DATA SHEET

Highest strength, standard modulus fiber available with excellent processing characteristics for filament winding and prepreg. This never twisted fiber is used in high tensile applications like pressure vessels, recreational, and industrial.

F I B E R   P R O P E R T I E S

	English	Metric	Test Method
Tensile Strength	711 ksi	4,900 MPa	TY-030B-01
Tensile Modulus	33.4 Msi	230 GPa	TY-030B-01
Strain	2.1 %	2.1 %	TY-030B-01
Density	0.065 lbs/in^3	1.80 g/cm^3	TY-030B-02
Filament Diameter	2.8E-04 in.	7 µm	

Yield		English	Metric	Test Method
	6K	3,724 ft/lbs	400 g/1000m	TY-030B-03
	12K	1,862 ft/lbs	800 g/1000m	TY-030B-03
	24K	903 ft/lbs	1,650 g/1000m	TY-030B-03

Sizing Type			Test Method
& Amount	50C	1.0 %	TY-030B-05
	60E	0.3 %	TY-030B-05
	F0E	0.7 %	TY-030B-05

Twist	Never twisted

F U N C T I O N A L   P R O P E R T I E S

CTE	$-0.38 \ \alpha \cdot 10^{-6}/°C$
Specific Heat	0.18 Cal/g·°C
Thermal Conductivity	0.0224 Cal/cm·s·°C
Electric Resistivity	$1.6 \times 10^{-3} \ \Omega \cdot cm$
Chemical Composition: Carbon	93 %
Na + K	<50 ppm

C O M P O S I T E   P R O P E R T I E S *

	English	Metric	
Tensile Strength	370 ksi	2,550 MPa	ASTM D-3039
Tensile Modulus	20.0 Msi	135 GPa	ASTM D-3039
Tensile Strain	1.7 %	1.7 %	ASTM D-3039
Compressive Strength	215 ksi	1,470 MPa	ASTM D-695
Flexural Strength	245 ksi	1,670 MPa	ASTM D-790
Flexural Modulus	17.5 Msi	120 GPa	ASTM D-790
ILSS	13 ksi	9 kgf/mm^2	ASTM D-2344
90° Tensile Strength	10.0 ksi	69 MPa	ASTM D-3039

* Toray 250°F Epoxy Resin. Normalized to 60% fiber volume.

T O R A Y   C A R B O N   F I B E R S   A M E R I C A ,   I N C .

T700S

COMPOSITE PROPERTIES**

Tensile Strength	355 ksi	2,450 MPa	ASTM D-3039
Tensile Modulus	18.0 Msi	125 GPa	ASTM D-3039
Tensile Strain	1.7 %	1.7 %	ASTM D-3039
Compressive Strength	230 ksi	1,570 MPa	ASTM D-695
Compressive Modulus	--- Msi	--- GPa	ASTM D-695
In-Plane Shear Strength	14 ksi	98 MPa	ASTM D-3518
ILSS	15.5 ksi	11 kgf/mm^2	ASTM D-2344
90˚ Tensile Strength	10.0 ksi	70 MPa	ASTM D-3039

** Toray Semi-Toughened 350˚F Epoxy Resin. Normalized to 60% fiber volume.

See Section 4 for Safety & Handling information. The above properties do not constitute any warranty or guarantee of values.

These values are for material selection purposes only. For applications requiring guaranteed values, contact our sales and technical team

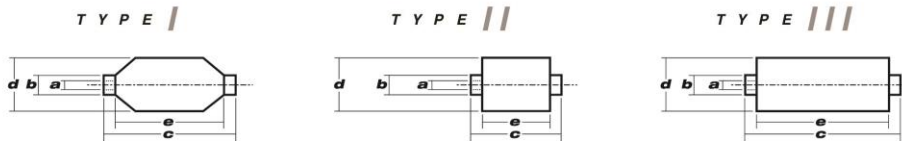to establish a material specification document.

PACKAGING

The table below summarizes the tow sizes, twists, sizing types, and packaging available for standard material. Other bobbin sizes may be available on a limited basis.

Tow Sizes	Twist[1]	Sizing	Bobbin Net Weight (kg)	Bobbin Type[2]	Bobbin Size (mm) a	b	c	d	e	Spools per Case	Case Net Weight (kg)
6K	C	50C	2.0	III	76.5	82.5	280	140	252	12	24
12K	C	50C	6.0	III	76.5	82.5	280	200	252	4	24
	C	60E	6.0	III	76.5	82.5	280	200	252	4	24
	C	F0E	6.0	III	76.5	82.5	280	200	252	4	24
24K	C	50C	6.0	III	76.5	82.5	280	200	252	4	24
	C	60E	6.0	III	76.5	82.5	280	200	252	4	24
	C	F0E	6.0	III	76.5	82.5	280	200	252	4	24

[1] **Twist**   A: Twisted yarn   B: Untwisted yarn made from a twisted yarn through an untwisting process   C: Never twisted yarn
[2] **Bobbin Type**   See Diagram below

TYPE I   TYPE II   TYPE III

Appendix B

Ciba

MATRIX SYSTEMS FOR AEROSPACE COMPOSITES
MATRIX SYSTEMS FOR INDUSTRIAL COMPOSITES

DATA SHEET

Hot curing epoxy system based on Araldite® LY 564 / Hardener HY 2954

Araldite LY 564 is a low-viscosity epoxy resin
Hardener HY 2954 is a cycloaliphatic polyamine

Applications	Wide range of industrial composites, aerospace composites
Properties	Due to the excellent handling behaviour the system is suitable for various production processes. It combines low viscosity with long pot life at elevated temperatures. The cured system shows excellent mechanical, dynamic and thermal (hot/wet) properties and good chemical resistance.
Processing	Resin Transfer Moulding (RTM) Filament Winding Pressure Moulding Pultrusion Wet lay-up

Key data

Araldite LY 564

Aspect (visual)	clear liquid	
Colour (Gardner, ISO 4630)	1 - 2	
Viscosity at 25 °C (ISO 9371B)	1200 - 1400	[mPa s]
Density at 25 °C (ISO 1675)	1.1 - 1.2	[g/cm^3]
Flash point (ISO 2719)	185	[°C]
Storage temperature (see expiry date on original container)	2 - 40	[°C]

Hardener HY 2954

Aspect (visual)	clear liquid	
Colour (Gardner, ISO 4630)	≤ 2	
Viscosity at 25 °C (ISO 9371B)	70 - 120	[mPa s]
Density at 25 °C (ISO 1675)	0.94 - 0.95	[g/cm^3]
Flash point (ISO 2719)	173	[°C]
Storage temperature (see expiry date on original container)	18 - 40	[°C]

Storage

Provided that Araldite LY 564 and Hardener HY 2954 are stored in a dry place in their original, properly closed containers at the above mentioned storage temperatures they will have the shelf lives indicated on the labels.

Partly emptied containers should be closed immediately after use.

Hardener HY 2954 which has crystallized and looks cloudy can be restored to its original state by heating to 70 - 80 °C.

January 1998

Mix ratio	Components	Parts by weight	Parts by volume
	Araldite LY 564	100	100
	Hardener HY 2954	35	42

We recommend that the components are weighed with an accurate balance to prevent mixing inaccuracies which can affect the properties of the matrix system. The components should be mixed thoroughly to ensure homogeneity. It is important that the side and the bottom of the vessel are incorporated into the mixing process.

When processing large quantities of mixture the pot life will decrease due to exothermic reaction. It is advisable to divide large mixes into several smaller containers.

Initial mix viscosity (Hoeppler, ISO 9371B)	[°C]		[mPa s]
	at 25		500 - 700
	at 40		200 - 300
	at 60		70 - 130

Viscosity build-up (Hoeppler, ISO 9371B)	[°C]	[mPa s]	[min]
	at 25	to 1500	150 - 180
	at 40	to 1500	100 - 130

Pot life (Tecam, 100 ml, 65 % RH)	[°C]		[min]
	at 23		480 - 600
	at 40		140 - 160

Gel time (Hot plate)	[°C]		[min]
	at 60		90 - 120
	at 80		35 - 45
	at 100		16 - 18
	at 140		3 - 4

The values shown are for small amounts of pure resin/hardener mix. In composite structures the gel time can differ significantly from the given values depending on the fibre content and the laminate thickness.

Processing recommendation

The temperature where gelation is being carried out should not be higher than necessary. A high gelation temperature induces shrinkage and generates internal stress within the part.

Typical cure cycles

2 h 60 °C + 4 - 8 h 120 °C
or 1 h 80 °C + 2 - 8 h 140 °C
or 0.5 h 100 °C + 2 - 8 h 160 °C

The optimum cure cycle has to be determined case by case depending on the processing and the economic requirements.

Properties of the cured, neat formulation

Glass transition temperature (T_G) (IEC 1006, 10 K/min)	Cure:		T_G (TMA) [°C]	T_G (DSC) [°C]
	4 h 80 °C		80 - 87	99 - 105
	1 h 80 °C + 4 h 120 °C		123 - 130	130 - 133
	1 h 80 °C + 8 h 120 °C		127 - 135	132 - 137
	1 h 80 °C + 12 h 120°C		134 - 139	138 - 142
	1 h 80 °C + 2 h 140 °C		123 - 127	129 - 134
	1 h 80 °C + 8 h 140 °C		140 - 144	143 - 148
	1 h 80 °C + 2 h 160 °C		128 - 135	134 - 142
	1 h 80 °C + 4 h 160 °C		136 - 143	143 - 150
	1 h 80 °C + 8 h 160 °C		145 - 149	150 - 153

Tensile test (ISO 527)	Cure:		1 h 80 °C + 8 h 140 °C	1 h 80 °C + 4 h 160 °C
	Tensile strength	[MPa]	71 - 77	78 - 82
	Elongation at tensile strength	[%]	4.5 - 5.5	6.3 - 7.3
	Ultimate strength	[MPa]	71 - 77	78 - 82
	Ultimate elongation	[%]	4.5 - 5.5	6.3 - 7.3
	Tensile modulus	[MPa]	2550 - 2650	2450 - 2550

Flexural test (ISO 178)	Cure:		1 h 80 °C + 8 h 140 °C
	Flexural strength	[MPa]	120 - 124
	Ultimate elongation	[%]	6.5 - 7.5
	Flexural modulus	[MPa]	2600 - 2800

Fracture properties Bend notch test (PM 258-0/90)	Cure:		1 h 80 °C + 8 h 140 °C
	Fracture toughness K_{1C}	[MPa$\sqrt{m}$]	0.69 -0.76
	Fracture energy G_{1C}	[J/m^2]	149 - 181

Water absorption (ISO 62)	Immersion:	Cure:	1 h 80 °C + 8 h 140 °C
	10 days H_2O 23 °C	[%]	0.23
	1 h H_2O 100 °C	[%]	0.20

Coefficient of linear thermal expansion (DIN 53 752)		Cure:	1 h 80 °C + 8 h 140 °C
	Mean value up to 80 °C	[10^{-6}/K]	70 - 75

Poison's ratio		[ ]	0.35

Properties of the cured, reinforced formulation

Interlaminar shear strength (ASTM D 2344)	Short beam: E-glass unidirectional specimen Laminate thickness t = 3.2 mm Fibre volume content: 60 %		
		Cure:	*1 h 80 °C + 8 h 140 °C*
	Shear strength	[MPa]	59 - 63
Tensile, Compressive and Torsional test (TCT)	Test specimen Roving: E-glass, 1200 tex, silane finish Fibre volume content: 63-65 %		
	Transverse tensile test	*Cure:*	*1 h 80 °C + 8 h 140 °C*
	Tensile strength Tensile strain Elastic modulus	[MPa] [%] [MPa]	43 - 49 1.8 - 2.0 15700 - 15900
	Transverse compressive test	*Cure:*	*1 h 80 °C + 8 h 140 °C*
	Compressive strength Elastic modulus	[MPa] [MPa]	110 - 140 15500 - 16000
	Torsional test	*Cure:*	*1 h 80 °C + 8 h 140 °C*
	Shear strength Shear modulus	[MPa] [MPa]	60 - 64 5000 - 6000

Handling precautions Mandatory and recommended industrial hygiene procedures should be followed whenever our products are being handled and processed. For additional information please consult the corresponding product safety data sheets and the brochure "Hygienic precautions for handling plastics products" (Publ. No. 24264/e).

Personal hygiene

Safety precautions at workplace

protective clothing	yes
gloves	essential
arm protectors	recommended when skin contact likely
goggles/safety glasses	yes

Skin protection

before starting work	Apply barrier cream to exposed skin
after washing	Apply barrier or nourishing cream

Cleansing of contaminated skin

Dab off with absorbent paper, wash with warm water and alkali-free soap, then dry with disposable towels. Do not use solvents

Disposal of spillage

Soak up with sawdust or cotton waste and deposit in plastic-lined bin

Ventilation

of workshop	Renew air 3 to 5 times an hour
of workplaces	Exhaust fans. Operatives should avoid inhaling vapours

First aid Contamination of the *eyes* by resin, hardener or mix should be treated immediately by flushing with clean, running water for 10 to 15 minutes. A doctor should then be consulted.

Material smeared or splashed on the *skin* should be dabbed off, and the contaminated area then washed and treated with a cleansing cream (see above). A doctor should be consulted in the event of severe irritation or burns. Contaminated clothing should be changed immediately.

Anyone taken ill after *inhaling* vapours should be moved out of doors immediately.

In all cases of doubt call for medical assistance.

Appendix C

Material properties for conventional steel:

Overview of materials for Low Alloy Steel

|	
Categories:	Metal; Ferrous Metal; Alloy Steel; Low Alloy Steel
Material Notes:	This property data is a summary of similar materials in the MatWeb database for the category "Low All minimum and maximum values of appropriate MatWeb entries. The comments report the average value, average. The values are not necessarily typical of any specific grade, especially less common values all processing methods.
Vendors:	No vendors are listed for this material. Please click here if you are a supplier and would like information

Physical Properties	Metric	English
Density	7.50 - 8.08 g/cc	0.271 - 0.292 lb/in³
Particle Size	6.70 - 12.0 µm	6.70 - 12.0 µm

Mechanical Properties	Metric	English
Hardness, Brinell	121 - 578	121 - 578
Hardness, Knoop	140 - 875	140 - 875
Hardness, Rockwell B	45.0 - 112	45.0 - 112
Hardness, Rockwell C	10.0 - 66.0	10.0 - 66.0
Hardness, Vickers	36.0 - 848	36.0 - 848
Tensile Strength, Ultimate	180 - 2730 MPa	26100 - 396000 psi
Tensile Strength, Yield	110 - 2400 MPa	16000 - 347000 psi
Elongation at Break	1.00 - 37.0 %	1.00 - 37.0 %
Elongation at Yield	1.00 - 40.0 %	1.00 - 40.0 %
Reduction of Area	3.00 - 75.0 %	3.00 - 75.0 %
Modulus of Elasticity	183 - 213 GPa	26500 - 30900 ksi
Compressive Yield Strength	1650 - 1800 MPa	239000 - 260000 psi
Bulk Modulus	140 - 170 GPa	20300 - 24700 ksi
Poissons Ratio	0.270 - 0.300	0.270 - 0.300
Fatigue Strength	138 - 772 MPa	20000 - 112000 psi
Fracture Toughness	80.9 - 143 MPa-m½	73.7 - 130 ksi-in½
Machinability	40.0 - 75.0 %	40.0 - 75.0 %
Shear Modulus	70.0 - 82.0 GPa	10200 - 11900 ksi
Izod Impact	9.00 - 138 J	6.64 - 102 ft-lb
Charpy Impact	15.0 - 339 J	11.1 - 250 ft-lb
Charpy Impact, Unnotched	39.3 - 176 J	29.0 - 130 ft-lb
Bend Radius, Minimum	0.000 - 4.00 t	0.000 - 4.00 t

Appendix D

Section picking in Abaqus; red section: plug-end, blue section: midsection and green section: lid-end.
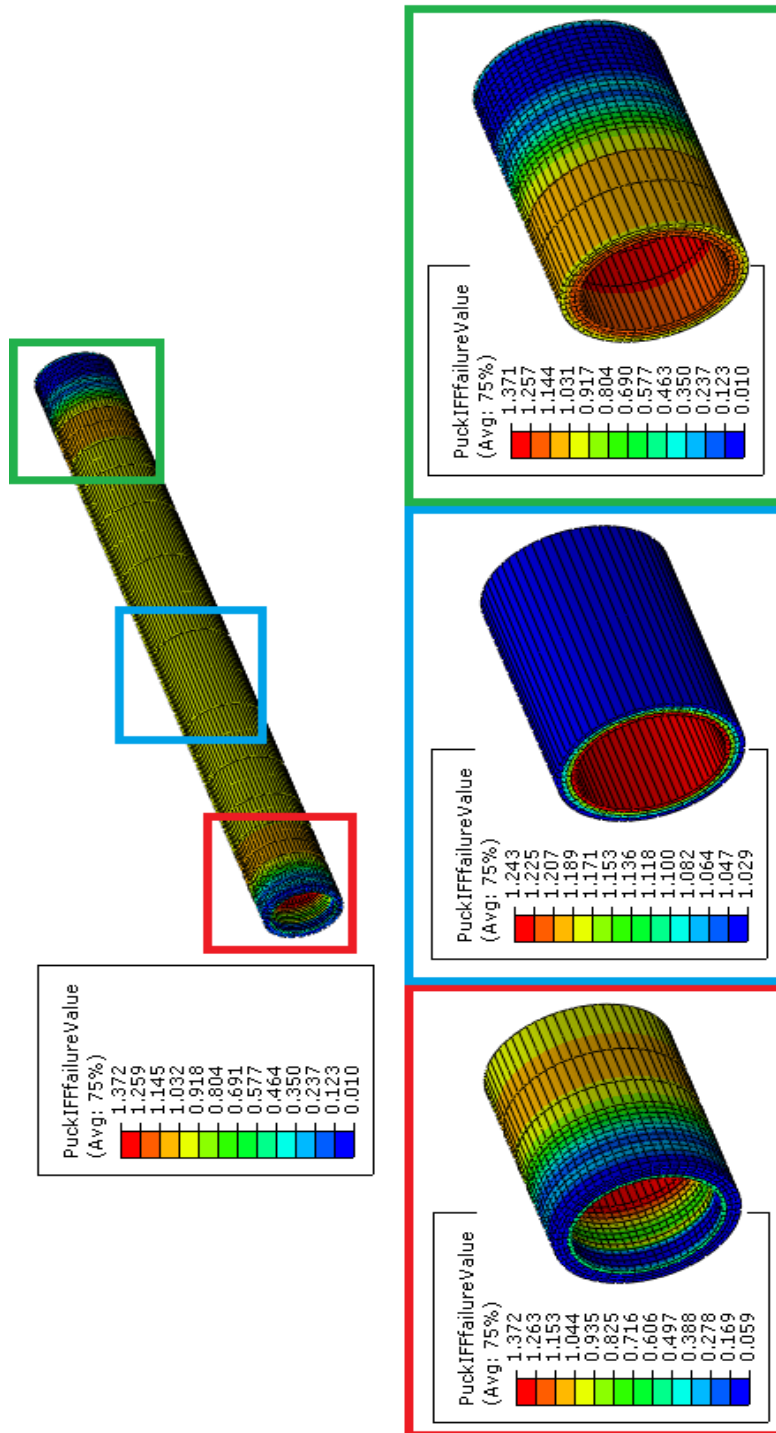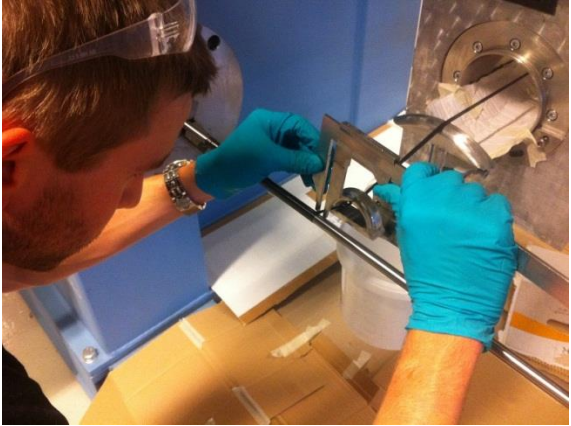
Appendix E

Pictures from test sample production:

Winding fibers on the mandrel

Measuring bandwidth

The first curing cycle was done with an oven placed over the rod, and a steel cover to prevent heat loss.
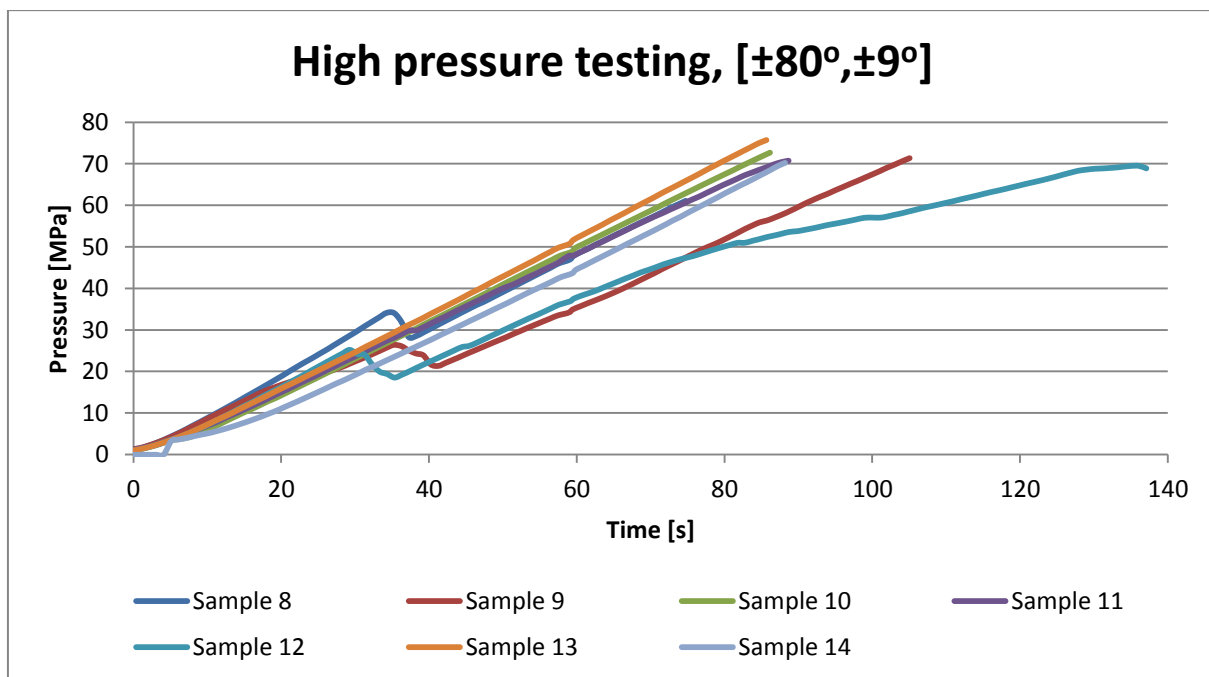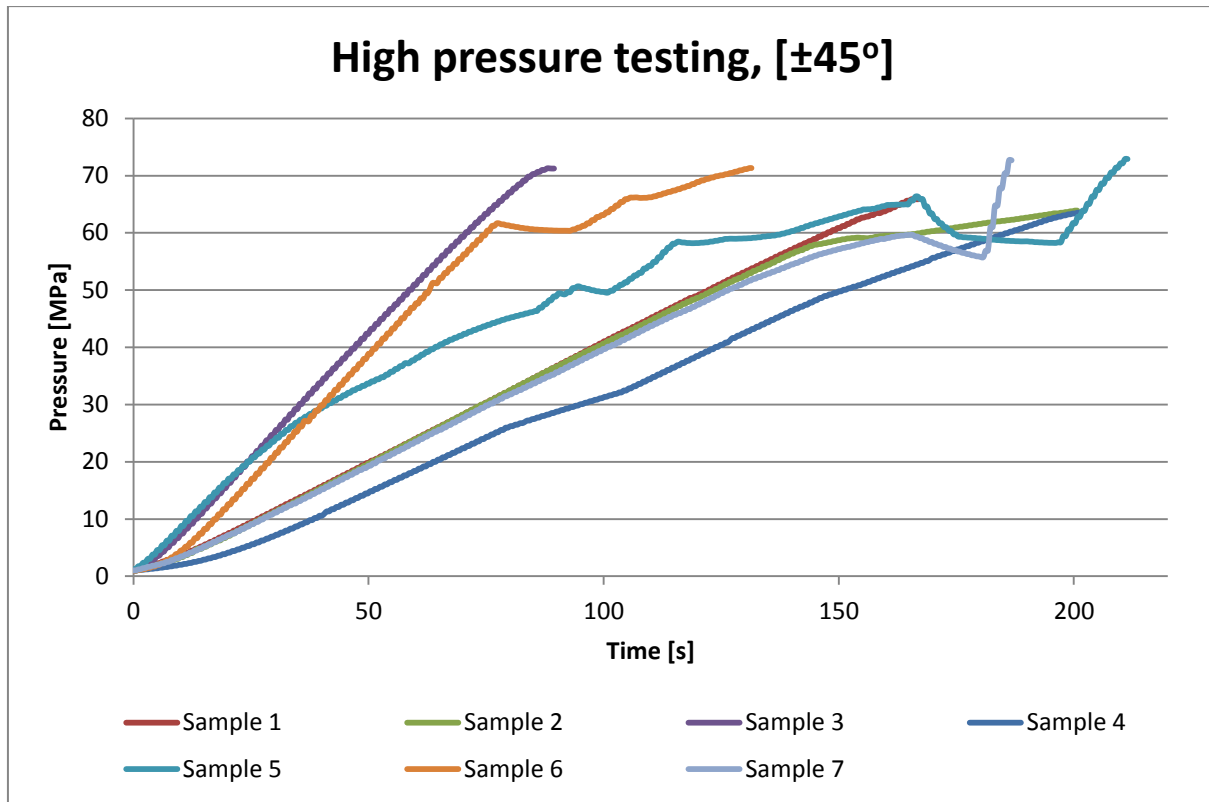

Winding the [±45°] layup

Winding the [±80°, ±9°] layup

Appendix F

Time-pressure curves for high pressure testing:

High pressure testing, [±45º]

High pressure testing, [±80º,±9º]

High pressure testing, [±80º]